博士論文

Structure dependent thermal transport properties of single walled carbon nanotubes

（単層カーボンナノチューブの構造依存熱輸送特性）

冯 雅

（Feng Ya）

Doctoral Dissertation

Structure dependent thermal transport properties of single walled carbon nanotubes

by

Ya FENG

Presented to

GRADUATE SCHOOL OF ENGINEERING, THE UNIVERSITY OF TOKYO

in Partial Fulfillment of the Requirements for the Degree of

Doctoral of Philosophy

in the Field of Mechanical Engineering

ABSTRACT

Since the discovery of carbon nanotubes in 1991 by Iijima, many potential applications have been suggested and examined in mechanics, optics, electronics and thermotics. Due to the quasi-one-dimensional atomic structure, individual carbon nanotube possesses significant thermal conductivity along the axial direction, thus its probable prospects in the field of thermal managements has attracted many researchers and engineers, especially as a thermal interface material to enhance the heat dissipation in electronics that limits the further miniaturization. Besides, the newly developed methods have fabricated high-quality free-standing carbon nanotube thin films, and they inherit some of the extraordinary characteristics and manifest great optical, mechanical, electrical and thermal properties as well.

Waste heat utilization has attracted worldwide attention due to the pressing energy crisis, hence thermoelectric materials owe to its simple and direct conversion from low-grade waste heat into high-grade electric power stand out as a promising candidate to ease the severe problem of this century. Of the current commercially available TE materials, the high cost, toxicity, inflexibility, and heavy weight are the obstacles for their broad applications. Therefore, extensive researches have been invested in organic TE materials that are cheaper, non-toxic, flexible and lighter, among which carbon nanotube thin film shows its great potential thanks to its abundance in nature and superb mechanical properties. Although the thermal conductance of individual carbon nanotubes is significantly high, the weak van der Waals interactions between nanotubes and the finite length of carbon nanotubes in network are hugely suppressing the thermal

conductance of the thin mats or films, while its electrical properties has not been affected much. Contrast to the easiness of obtaining the electrical properties of carbon nanotube thin films with well-studied theories and experiments, the thermal properties on the other hand are short of fairly verified methods to account for. Therefore, this thesis proposes a new method for studying the in-plane thermal conductance of thin film with infrared thermography. Infrared thermography is a quick method to obtain the temperature profiles of the targets, along with some ad hoc designing to calculate the heat flux, it can develop into a direct and handy technique for contactless thermal conductance determination. In this experiment, the single walled carbon nanotube thin films are free-standing in between two cantilevered silicon thin plates which work as the reference to calculate the heat flux through SWNT thin film. The temperature profile along the silicon-SWNT-silicon bridge is recorded with the infrared camera. Besides, another unloaded parallel silicon pair is set in order to offset the noise from the camera. A control experiment without film is also conducted to account for background conductance originating from thermal radiation or residual convection. Since the thickness of single walled carbon nanotube thin film in this study is hard to determine and it is changeable under different conditions, sheet thermal conductance is proposed to evaluate the capability of heat transfer of single walled carbon nanotube thin films. The results indicate the sheet thermal conductance are 15613.4 ± 2672.5nW/K, 9925.4±1417.1nW/K, 5454.8±594.9nW/K and 3405.7±773.8nW/K at room temperature for single walled carbon nanotube thin film with transparency of 60%, 70%, 80% and 90%, respectively. Furthermore, for the 50nm single walled carbon nanotube thin film of 90% transparency, its thermal conductivity is around 68.1$Wm^{-1}K^{-1}$, which is benefitting from the composition of the very long high-quality single walled carbon nanotubes by aerosol chemical

vapor deposition synthesis method. The sensitivity of This method is on the order of 10^{-6} W/K and can be applied to any other films (especially low thermal conductance films) that can be transferred to free-standing in between the cantilevered silicon pair plates. Besides, in comparison with the Raman measurements performed on the same thin films, the non-equilibrium among different phonon polarizations in Raman measurements might have contributed to the lower sheet thermal conductance by a factor of 1.9 to 2.5 in the condition of this study.

There has been large amount of experiments conducted concerning the axial thermal conductivity of individual carbon nanotubes. However, the various sample preparation methods as well as different measurement methods make the results ranging hugely and hardly comparable with each other. The hidden reason behind this challenge is the difficulty to identify the precise nanoscale structure of the carbon nanotubes being studied. Furthermore, the chirality-specific SWNT growth has been realized, which have excited the application in electronics, then the thermal behaviors of individual single walled carbon nanotubes with specific atomic structure are more urgently needed to be addressed. Besides, the length of SWNT is a critical parameter that determines the number of phonons in it, but the length dependency of phonon conductance in single walled carbon nanotubes is still a controversial debate in theoretical investigations, and due to the challenges of sample preparations, there are scarce experimental studies to clarify the disagreement. The unsettlement and insufficiency of the structure dependency of thermal transport properties in SWNTs motivate us to systematically study the relationship of the thermal conductance and its nanoscale structure with the high-quality defect-free horizontally aligned

SWNTs. Tackling the structure dependency of thermal transport in individual SWNTs would help us better understand and manipulate its extraordinary thermal properties to serve for future applications.

The micro-thermometer compatible with transmission electron microscope has been fabricated in this thesis to investigate the axial thermal conductance of individual carbon nanotubes and their nanoscale structure. The transmission electron microscope images show that the transferred horizontally aligned carbon nanotubes across the micro-thermometers are very clean and straight. Through comparison of the SEM and TEM images, the number of SWNTs in a bundle can be determined by counting the extended SWNTs dispersedly distributed on the supporting membranes. The thermal conductance of four samples, including three bundles with different sizes as well as three isolated single carbon nanotubes, have been studied. Thanks to the very long extended carbon nanotubes on the membranes and the annealing process during carbon nanotube transfer, the contact strength and contact area is immensely enhanced that the thermal boundary resistance can be effectively ignored in this investigation. The measured background conductance is much higher than the theoretical prediction, makes the deduction of background conductance compulsory for the precision of measurements. The effective thermal conductivity of the four samples under investigation are increasing with the temperature first and saturates around room temperature. The thermal conductivity of the isolated carbon nanotubes reaches around $5000 Wm^{-1}K^{-1}$ around 300K, fold larger than that of the bundles. Furthermore, the larger the size of the bundles, the lower its effective thermal conductivity. The logarithmical decrease of the thermal conductivity with the bundle size is the first-time quantitative study. This

experiment proves the serious degeneration of thermal transport properties by the interactions between carbon nanotubes, and in consistent with the IR measurements of higher thermal conductivity of thin films composed of smaller size bundles.

In macro-scale, a quick and handy method is presented here to measure the sheet thermal conductance of carbon nanotube thin films; in nanoscale, the correlation between the thermal transport properties of individual carbon nanotube and its nanoscale structure is investigated to provide scientific guides to carbon nanotube electronics architecture. Therefore, the clear relationship of the thermal conductivity of carbon nanotube and its nanoscale structure can help to design the thermal conductance of carbon nanotube thin films through control growth, tuning it to be higher for thermal managements or lower for insulator or thermoelectric applications in the future.

CONTENTS

CHAPTER 1 INTRODUCTION

1.1 BACKGROUD

Heat dissipation in electronics is the bottleneck in this ever-pursuing miniaturization century, urgently needs to be broken through[1]. The extraordinary axial thermal transport capabilities of single walled carbon nanotube (SWNT)[2] makes it a promising candidate for thermal managements in micro- or nano-scale devices. Therefore, how to control and manipulate the ultra-high thermal transport properties of SWNT to serve for applications in reality calls for more precise investigations concerning to the intrinsic thermal transport properties of SWNT as well as their dependencies on other factors, such as its geometrical parameters and the future working conditions.

Researches have extensively conducted on the thermal transport properties of carbon nanotubes (CNTs) through theoretical[3-7] and experimental[8-17] studies in the past score years, as indicated in Table 1-1. However, due to the various sample preparations and methodologies, the results from different researches can hardly be compared with each other to enhance or degrade the conclusions[18], and this dilemma mostly lies to the difficulty of identification of the precise structure of SWNTs being investigated. As shown in Table 1-1, the values of thermal conductivities of CNT ranges from tens to thousands from experiments, and the similar phenomena is also exhibited in the simulation studies. Even from the same group of researchers, different samples vary largely in their capability of heat transfer[19]. Besides, when the one-dimensional individual SWNTs form multi-dimensional bundles or bulky mats or films, their

thermal transport properties change a lot, even becoming a good insulator[20]. Those are indicating that the atomic structure of SWNTs or formation structure of SWNT films possess a great influence on their thermal transport properties.

Table 1-1 Reported thermal conductivities for SWNTs, MWNTs and CNT films or mats by experiments.

Experimental thermal measurements of CNTs							
SWNTs			**MWNTs**			**Films or Mats**	
L (μm)	D (nm)	κ ($Wm^{-1}K^{-1}$)	L (μm)	D (nm)	κ ($Wm^{-1}K^{-1}$)	Thickness (nm)	κ ($Wm^{-1}K^{-1}$)
41	1.8	2400[17]	32	8.2	1400[17]	93000~55	0.203~65.9[21]
2.6	1.7	3436[15]	2.5	14	3000[13]	170	18.3[22]
2.76	1-3	3270-9800[14]	1 /1.1	46 /42	650 /830[8]	140	50[23]
4.31 /2.03	2.34 /1.5	~500 /600[19]	1.4	20	300[10]	400~500	80~370[24]
0.509 /4.919/ 6.941	1.9 /1.9 /1.9	2630 /3160 /3210[16]	4.02 /3.02 /1.95 /1.97 /3.31	2.7 /10.3 /9.9 /11.4 /14.0	~ 520 /210 /180 /130 /34[19]	1300	>200[25]
2/ 1039	2 /2	2700 /8638[26]	3.7 /1.89 /3.6	9.8 /16.1 /28.2	2950 /1650 /500[9]	87	16.5[27]

As followed, the physics of this unique material of our topic will be introduced, including its geometrical structure which is what we are pursuing to identify in our experiments, its electronic properties which burdens part of the heat transfer and its phonon modes that is the main heat carriers. Then the thermal transport mechanism in SWNTs will be briefed. Lastly, the current thermal conduction metrology for SWNTs will be presented.

1.2 PHYSICS OF CARBON NANOTUBES

Carbon is the elementary of all life on the earth, and itself with different atomic architectures can form different materials with very different properties. For example, the diamond, one of the common allotrope of carbon is the hardest material, while graphite, another allotrope of carbon is so soft that it is the composition of our daily pencil for writing and drawing. Besides, carbon fibers with strong mechanical properties are widely used in the aerospace, civil engineering and military. Except the above bulk materials, carbon allotropes include the two-dimensional (2D) graphene, which is the layer unit of graphite and won Noble Prize for Chemistry in 2005, one-dimensional (1D) carbon nanotubes and zero-dimensional (0D) fullerenes.

To some extent, ever since humans learnt to make fire, we were making fullerenes and CNTs. Fullerenes are a small part of the carbon particles in the flames. However, it is until 1985 that humans are consciously entering the carbon nano world with the discovery of fullerene[28], which won the Noble Prize for Chemistry in 1996. After that, people started to infer that CNT were some limited geometry of spherical fullerene, so CNT was the most important adds-on for the study of fullerene. In 1991, the Japanese scientist Iijima observed the multi-walled carbon nanotubes (MWNT) in NEC lab for the first time[29], which hugely promoted the science academia to the field of CNT, and two years later in 1993, SWNT was discovered[30].

A SWNT is formed when a two-dimensional single layer graphene sheet is rolled seamless into a cylinder; if it is multi-layered graphene sheets that roll up, it will generate an MWNT. SWNT has been theoretically predicted with extraordinary characteristics in mechanics, electronics, optics and thermotics dues to its quasi-one-dimensional structure even before its preparation has been realized. Later, the development of growth methods such as arch-discharge, laser ablation, plasma torch, and chemical vapor deposition (CVD) have rapidly produced large scale CNTs[31, 32], narrowing the gap between theoretical predictions to realistic applications.

1.2.1 GEOMETRICAL STRUCTURE

To better understand the geometry of SWNT, the lamellar structure of graphite (graphene sheet) is a good start point[33]. Graphite is stacked with graphene sheets which is composed of sp^2 hybridized carbon atoms arranged in repeatable hexagons. When a single layer 2D graphene sheet is rolled seamless into a cylinder, a particular SWNT is generated, defined by the rolling vector or chiral vector $\mathbf{C_h}$. There are three general types of SWNTs according to their rolling vector: zigzag, armchair and chiral, shown in the Figure 1-1. Zigzag and armchair refer to the end shape of the carbon nanotube and they are highly symmetrical, while the chiral ones are common and abundant.

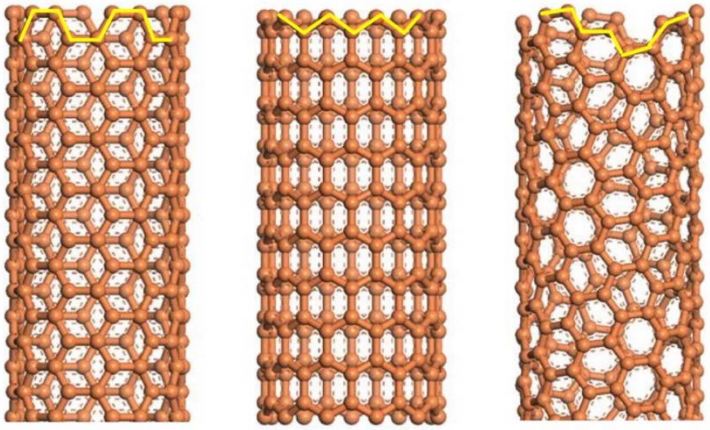

FIG. 1-1 Left: (6, 6) armchair SWNT; Middle: (11, 0) zigzag SWNT; Right: (8, 5) chiral SWNT. The end shapes are highlighted to show the origin of the names.

The rolling vector, also known as chirality is the only definition of SWNT, it completely determines the structural parameters of SWNTs, such as diameter, crystal units, number of carbon atoms, as well as the size and shape of Brillouin zone. It can be expressed as $\mathbf{C_h} = n\mathbf{a_1} + m\mathbf{a_2} \equiv (n, m)$, in which $\mathbf{a_1}$ and $\mathbf{a_2}$ are the unit vectors of graphene, n and m are integers. The length of the unit vector is $|\mathbf{a_1}| = |\mathbf{a_2}| = a = 2.416$Å, and a is the lattice constant of graphene, and the cross angle of the two unit-vectors is 60°. When the graphene sheet was rolling into a seamless cylinder, the start-point and end-point of $\mathbf{C_h}$ is in superposition, so the circumference of the SWNT is $|\mathbf{C_h}|$, then the diameter of SWNT d_t can be calculated by the following equation.

$$d_t = |\mathbf{C_h}|/\pi = a \cdot \sqrt{m^2 + m \cdot n + n^2}/\pi \qquad \text{Eq. (1-1)}$$

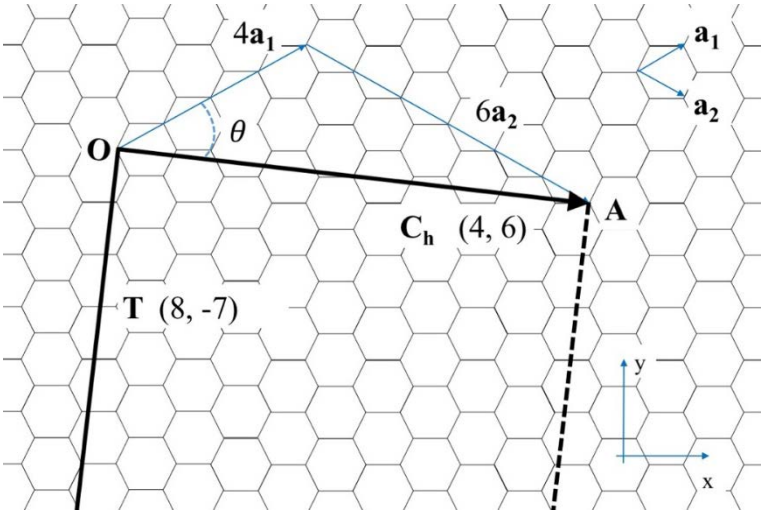

FIG. 1-2 Lattice structure of graphene; how to roll the graphene sheet into a (4, 6) SWNT (the translational vector T is truncated for space consideration).

By the above definition, the SWNT is exclusively identified by the integer pair (*n*, *m*), which is named as chirality of the SWNT. To be more illustrative, Figure 1-2 generates a (4, 6) SWNT, the starting **O** and ending **A** of the chiral vector will match together when the graphene sheet rolls seamlessly. Besides, when *m*=0 or *n*=0, the generated SWNTs are zigzags, while when *n*=*m*, it all belongs to the armchair. The chiral angle θ is defined as the cross angle of $\mathbf{a_1}$ and $\mathbf{C_h}$, which can be calculated through Equation (1-2).

$$\theta = \tan^{-1}\left|-\sqrt{3}\cdot n/(2m+n)\right| \qquad \text{Eq. (1-2)}$$

The vector **T**, perpendicular to $\mathbf{C_h}$, is the smallest lattice vector in graphene sheet that determines the axial translational period of the SWNT, which can be expressed by integer pair (t_1, t_2) that are related to chirality (*n*, *m*).

$$\mathbf{T} = \frac{2m+n}{d_R}\mathbf{a_1} - \frac{2n+m}{d_R}\mathbf{a_2} = t_1\mathbf{a_1} + t_2\mathbf{a_2} \equiv (t_1, t_2) \qquad \text{Eq. (1-3)}$$

$$T = |\mathbf{T}| = \frac{\sqrt{3(n^2+nm+m^2)}}{d_R}a \qquad \text{Eq. (1-4)}$$

here, d_R is the largest common divisor of ($2n+m$) and ($2m+n$).

$$d_R = \begin{cases} d, & \text{if n} - \text{m is not a multiple of 3d;} \\ 3d, & \text{if n} - \text{m is a multiple of 3d;} \end{cases} \quad \text{Eq. (1-5)}$$

where d is the largest common divisor of n and m. Therefore, the lattice unit of SWNT is composed of the surface of a cylinder with diameter of d_t and height of T. For the zigzag and armchair SWNTs, the above formulas can be simplified as

$$|\mathbf{C_h}| = na, \quad T = \sqrt{3}a, \quad \theta = 0 \qquad \text{(Zigzag)} \qquad \text{Eq. (1-6)}$$

$$|\mathbf{C_h}| = \sqrt{3}na, \quad T = a, \quad \theta = 30° \qquad \text{(Armchair)} \qquad \text{Eq. (1-7)}$$

The number of carbon atoms N_c in the lattice unit can be calculated by the ratio of the surface area of the lattice unit cylinder, which is $S_t = T \cdot \pi d_t$ and the lattice area of graphene S_g. Moreover, this ratio provides the number of hexagons in the lattice unit of SWNT N,

$$N = \frac{S_t}{S_g} = \frac{2(n^2+nm+m^2)}{d_R} \quad \text{Eq. (1-8)}$$

Since there are two carbon atoms in the hexagon, the number of carbon atoms in the lattice unit of SWNT is

$$N_c = 2N = \frac{S_t}{S_g} = \frac{4(n^2+nm+m^2)}{d_R} \quad \text{Eq. (1-9)}$$

To the zigzag and armchair, from the above equation it can be readily deduced that there are $4n$ carbon atoms in their lattice units.

1.2.2 ELECTRONIC PROPERTIES

One of the most impressive characteristics of SWNTs is that they can be metallic or semiconducting depending on their chirality, and the band gap ranges from 0.5eV to 2eV which

covers most of the semiconductors current in use. A brief introduction to their unique electronic properties is also necessary to better understand the behavior of their counterpart, phonons, in heat transfer.

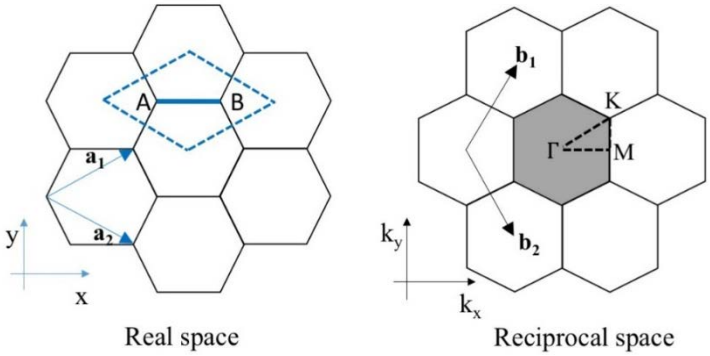

FIG. 1-3 The unit cell and Brillouin zone of graphene are indicated as the dotted rhombus and shaded hexagon in real space (left) and reciprocal space (right), respectively.

The unit cell of graphene in real space (lattice) and momentum space (reciprocal lattice) are shown in Figure 1-3. In the Cartesian *x*-*y* coordinate, the basis vectors $\mathbf{a_1}$ and $\mathbf{a_2}$ in real space are expressed as

$$\mathbf{a_1} = (\frac{\sqrt{3}}{2}a, \frac{1}{2}a), \quad \mathbf{a_2} = (\frac{\sqrt{3}}{2}a, -\frac{1}{2}a) \qquad \text{Eq. (1-10)}$$

and a is the lattice constant of graphene as introduced in the last section. Correspondingly, in the k_x-k_y coordinate, the basis vectors in the reciprocal lattice $\mathbf{b_1}$ and $\mathbf{b_2}$ are given by

$$\mathbf{b_1} = (\frac{2\pi}{\sqrt{3}a}, \frac{2\pi}{a}), \quad \mathbf{b_2} = (\frac{2\pi}{\sqrt{3}a}, -\frac{2\pi}{a}) \qquad \text{Eq. (1-11)}$$

and the lattice constant in reciprocal space is $4\pi/\sqrt{3}a$. In the Brillouin zone of graphene, three high symmetry points, Γ, K and M denoting the center, the corner, and the center of the edge are defined, respectively.

Similarly, since the basis vectors in real space of a SWNT is $\mathbf{C_h}$ and $\mathbf{T}$, the basis vectors in reciprocal space of it can be defined as $\mathbf{K_1}$ and $\mathbf{K_2}$ through the following equations.

$$\mathbf{C_h} \cdot \mathbf{K_1} = 2\pi; \quad \mathbf{T} \cdot \mathbf{K_1} = 0; \qquad \text{Eq. (1-12a)}$$

$$\mathbf{C_h} \cdot \mathbf{K_2} = 0; \quad \mathbf{T} \cdot \mathbf{K_2} = 2\pi. \qquad \text{Eq. (1-12b)}$$

Therefore, $\mathbf{K_1}$ and $\mathbf{K_2}$ can be obtained as

$$\mathbf{K_1} = \frac{1}{N}(-t_2 \cdot \mathbf{b_1} + t_1 \cdot \mathbf{b_2}) \qquad \text{Eq. (1-13a)}$$

$$\mathbf{K_2} = \frac{1}{N}(m \cdot \mathbf{b_1} - n \cdot \mathbf{b_2}) \qquad \text{Eq. (1-13b)}$$

As demonstrated in the above equations, the Brillouin zone of SWNT in momentum space is much smaller than that of graphene because of the much larger unit cell in its real space, and it becomes cutting lines on the reciprocal lattice of graphene as shown in Figure 1-4(a), which are results of the N wave vectors $\mu\mathbf{K_1}$ (μ=0, …, N-1). These leads to N discrete *k* vectors in the circumferential direction. For each of the μ discrete circumferential wave vectors, a one-dimensional electronic energy band appears, whereas each of them gives rise to 6 branches in the phonon dispersion relations. In the axial direction, if the length of SWNT is infinite, there would be continuous wave vectors along $\mathbf{K_2}$, while for SWNT with finite length of L_t, the distance between wave vectors is $2\pi/L_t$.

The allowable and discrete wave vectors in the circumferential direction of SWNT can

or cannot pass through the *K*-point of the 2D Brillouin zone of graphene depending on the chirality (*n*, *m*), where the valence and conduction bands are keeping in touch in graphene, thus resulting a metallic or semiconducting SWNT. With the increasing diameters, there are more allowable wave vectors for the circumferential direction, indicating that the CNTs are transforming from 1D to 2D, and the semiconducting band gap gradually disappears. Therefore, to observe 1D quantum effects, the CNTs have to be smaller enough in their diameters.

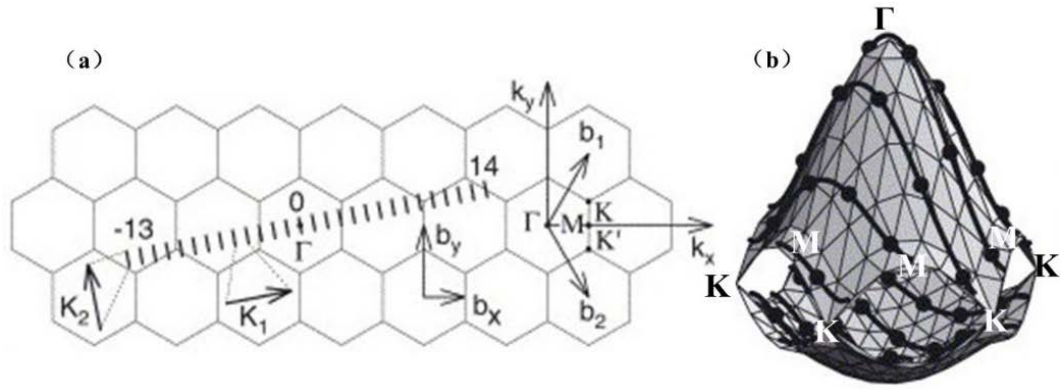

FIG. 1-4 (a) Brillouin zone (cutting lines) of (4, 2) SWNT in the lattice reciprocal of graphene; (b) The conduction and valence bands of a graphene layer in the first Brillouin zone and the cutting lines of (4, 2) SWNT indicated in solid lines (adapted from reference [34], Copyright 2005, with permission from Elsevier).

The cutting lines for a small SWNT with chirality of (4, 2) in the first Brillouin zone of graphene are obtained through tight-binding method and shown in Figure 1-4[34], as can be seen, its cutting lines have not come across the *K*-point, so (4, 2) is a semiconducting CNT. Besides, the electronic density of states (eDOS) can also be calculated, and in Figure 1-5, the eDOSs of semiconducting and metallic SWNTs give a general view of their origin of differences. The sharp

peaks in the eDOS is named as van Hove singularities (vHS) that is introduced by the one-dimensional quantum confinement. The eDOS of the metallic SWNT (9, 0) is nonzero at the Fermi level, while that of the semiconducting SWNT (10, 0) is zero and the energy difference between the first two vHSs crossing over the zero-area is the bandgap. Therefore, the 2D graphene is a zero-gap semiconductor, as the dotted lines in the figure (eDOS of graphene) touches the bottom but immediately increases. The calculation details are specified in Reference[34].

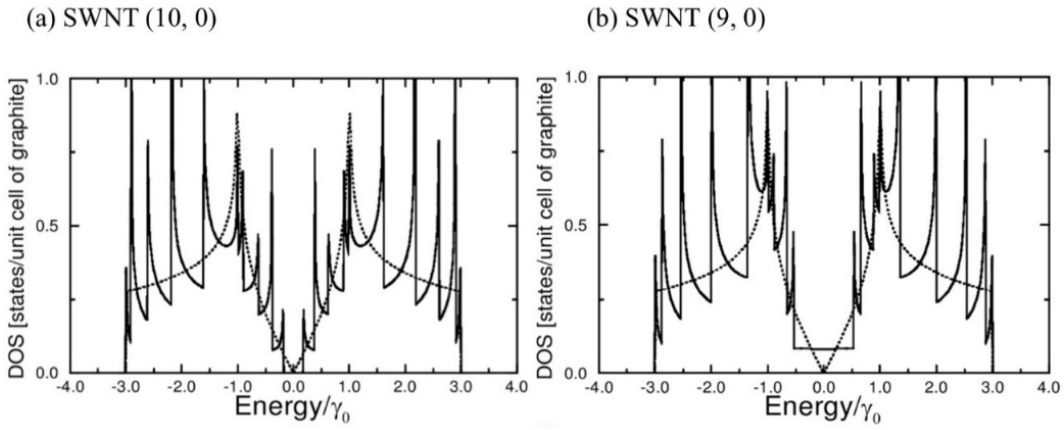

Figure 1-5 Electronic density of states of SWNTs, in which (a) is from a semiconducting SWNT (10, 0) and (b) is from a metallic SWNT (9, 0), also the dotted line in the figures is from the graphene sheet as in comparison (adapted from reference [35], Copyright 2000, with permission from Taylor & Francis).

Moreover, the calculations also revealed that one third of the nanotubes are metallic and the other two thirds are semiconducting according to their chirality. When the chirality of a SWNT satisfies $2n+m=3q$ (q is any integer), it is metallic, whereas it is semiconducting if not[33].

As a result, a periodic table of SWNTs based upon the electronic properties can be generated, as demonstrated in Figure 1-6.

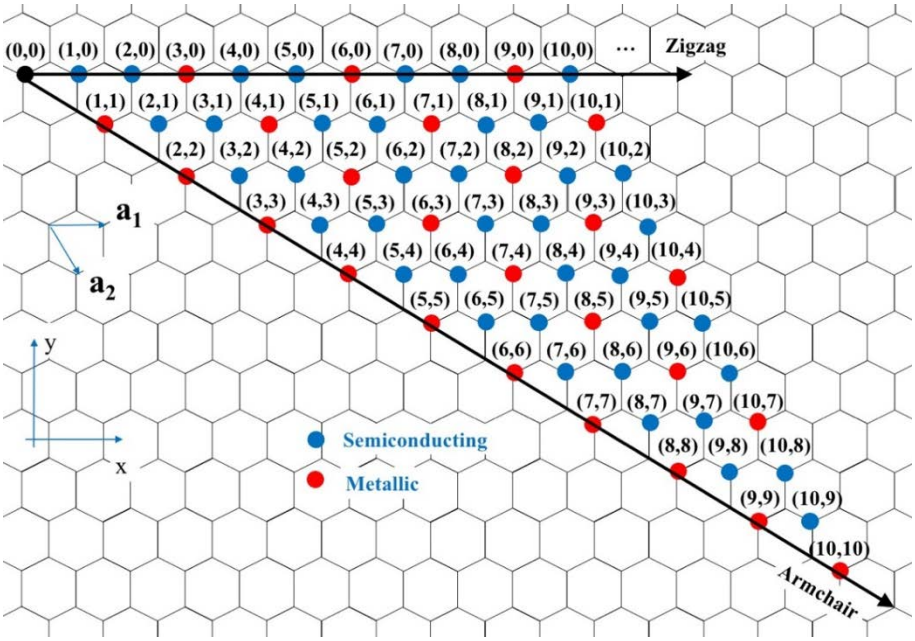

FIG 1-6 Periodic table of SWNTs. The blue dot indicating a semiconducting SWNT, while the red dot referring to a metallic SWNT.

1.2.3 PHONON MODES

The phonon dispersion relations in a SWNT can be obtained from those of the 2D graphene sheet through the same zone folding approach as mentioned in the electronic properties. Since there are $2N_c$ carbon atoms in the unit cell of a SWCNT, the total vibrational degree is $6N_c$, therefore the phonon dispersion relations of SWNT consist of $6N_c$ branches deriving from a vector displacement of each carbon atom in its unit cell.

The one-dimensional phonon dispersion relations $\omega_{1D}^{m\mu}(k)$for SWNTs are relating to that of two-dimensional graphene $\omega_{2D}^{m\mu}(k)$ through the following expression[35]:

$$\omega_{1D}^{m\mu}(k) = \omega_{2D}^{m\mu}(k)\left(k\frac{\mathbf{K}_2}{|\mathbf{K}_2|} + \mu\mathbf{K}_1\right), \begin{pmatrix} m = 1, \cdots, 6, \\ \mu = 0, \cdots, N-1, \end{pmatrix} and\ -\frac{\pi}{T} < k \leq \frac{\pi}{T} \quad \text{Eq. (1-14)}$$

The superscript *m* represents the 6 phonon modes originating from three-dimensional vibrations of the two carbon atoms in graphene unit cell, shown in Figure 1-7(a), in addition Figure 1-7(b) shows the corresponding phonon density of states; *k* is any one-dimensional wave vector, $\left(k\frac{\mathbf{K}_2}{|\mathbf{K}_2|} + \mu\mathbf{K}_1\right)$ describing the quantized wave vectors in the circumferential direction of SWNT resulting from the periodic boundary conditions.

Figure 1-7(c) demonstrates the calculated phonon dispersion relations of (10, 10) armchair SWNT. Although there are 120 degrees of freedom, only 66 phonon branches are recognizable due to the degeneracies of some modes. At the lower frequencies, there are four acoustic phonon modes around the Γ point that crossing at *k*=0, which are the doubly degenerate transverse acoustic (TA) modes, the longitudinal acoustic (LA) mode, and the twisting acoustic (TW) mode, respectively. These low-frequency acoustic phonon modes are significant for thermal transport in CNTs due to their relatively larger group velocity (dω/dk) and better coupling to the heat sink in comparison with the high-frequency optical modes[36]. Alongside, the phonon density of states for (10, 10) SWNT is shown in Figure 1-7(d), where a large number of peaks appears while no such exhibition in that of graphene, reflecting the unique effects from 1D quantum confinement.

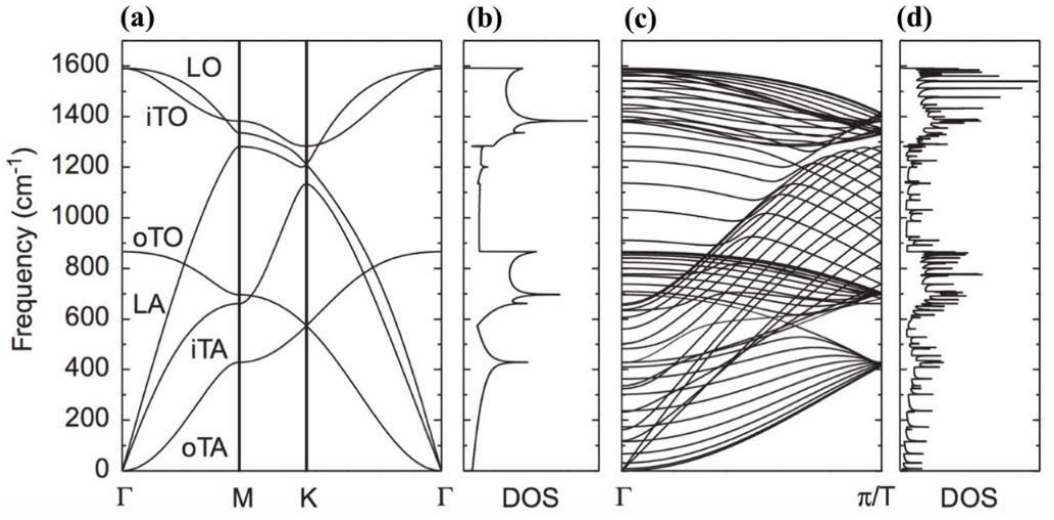

FIG 1-7 (a) Phonon dispersion relations of graphene sheet, including six phonon modes which are out-of-plane transverse acoustic (oTA), in-plane transverse acoustic (iTA), longitudinal acoustic (LA), out-of-plane transverse optic (oTO), in-plane transverse optic (iTO) and longitudinal optic (LO), respectively. (b) The phonon density of states of graphene sheet. (c) The calculated phonon dispersion relations of (10, 10) armchair SWNT. (d) The corresponding phonon density of states for (10,10) SWNT (adapted from reference [34], Copyright 2005, with permission from Elsevier).

1.3 THERMAL TRANSPORT IN CARBON NANOTUBES

Phonons are the dominant heat carriers in 3D crystalline diamond and graphite as well as 2D graphene sheet, and the contribution from electrons are small enough to be ignored. Therefore, phonons are expecting to be dominating in thermal transport of SWNTs which are derivatives of graphene sheets. The phonon contribution to the heat capacity is generally expressed as[35]:

$$C_{ph} = \int_0^{\infty} \frac{k_B\left(\frac{\hbar\omega}{k_B T}\right)^2 \rho(\omega) e^{\hbar\omega/k_B T} d\omega}{\left(e^{\hbar\omega/k_B T} - 1\right)^2} \qquad \text{Eq. (1-15)}$$

where $\rho(\omega)$ is the phonon density of states obtained from the phonon dispersion relations. For the isolated SWNTs, the four acoustic phonon modes which are mentioned in the last section, exhibiting a linear dispersion relation $\omega=vk$ at lower wave vectors (Figure (1-7c)) in the low temperature range, are expected to be the dominated heat carriers. Therefore, the phonon density of states is regarded as being independent of ω, and a linear relationship between C_{ph} and temperature T in the low range can be expected as:

$$C_{ph} = const\frac{k_B^2 T}{\hbar v},\ T \ll \frac{\hbar v}{k_B d_t}, \qquad \text{Eq. (1-16)}$$

Here, v and d_t are an appropriately averaged velocity of sound and the diameter of SWNT, respectively. Even though these four high-energy phonon modes weight significantly, the contribution from the optical phonons cannot be completely nullified and would bring the total heat capacity deviate from the linearity with temperature[37].

The contribution from the electrons to heat capacity is also considered to be in a linearity with temperature, particularly at lower temperature, in metallic SWNTs, but its impact is two orders of magnitude lower than phonons since the velocity of sound is hundred times larger than the Fermi velocity. As in semiconducting SWNTs, the electron contribution is quite small at lower temperature resulting from the disappearance of eDOS at Fermi Level and is expected to depend exponentially on temperature[35].

Electrons and phonons both contribute to heat transfer in SWNTs. Thermal conductivity from electrons can be determined from the electrical conductivity σ by the Wiedemann-Fanz law:

$$\frac{\kappa_{el}}{\sigma} \approx L_0 = 2.45 \times 10^{-8}\ (V/K)^2 \qquad \text{Eq. (1-17)}$$

In the one-dimensional limit, the phonon thermal conductivity can be expressed as:

$$\kappa_{ph} = \sum C v^2 \tau \qquad \text{Eq. (1-18)}$$

C, *v* and τ are specific heat capacity, phonon group velocity in the axial direction of SWNT and the relaxation time of a given phonon mode. The sum is conducted over all phonon modes. Thus, the total thermal conductivity of SWNTs can be obtained through summing κ_{el} and κ_{ph}. It is worth to note that the contribution to heat transfer from the phonons is much larger than that from the electrons at all temperatures in SWNTs. At low temperatures ($T \ll \Theta_D$, Debye temperature), the boundary or defect scattering dominates the inelastic phonon scattering, indicating that the changes in temperature should not affect the relaxation time τ, thus the phonon thermal conductivity would behave linearly with temperature as the heat capacity does in this temperature range. As temperature increases, the phonon-phonon Umklapp scattering start to populate and shorten the relaxation time τ, so that the linearity to temperature vanishes[38].

1.4 THERMAL CONDUCTION METROLOGY OF CARBON NANOTUBES

Driven by the promising prospects of 2D quantum wells and 1D quantum wires enhancing thermoelectric figure of merits ($ZT \equiv S^2\sigma T/\kappa$, where S, σ, κ and T are the Seebeck coefficient, electrical conductivity, thermal conductivity and absolute temperature, respectively), a number of thermoelectric characterization methods have been designed especially for thin films

and nanowires[39, 40], which also benefit for the thermal properties investigation of CNTs and CNT films.

1.4.1 3Ω METHOD

The 3ω method was initially designed by Cahill[41] to measure the cross-plane thermal conductivity of thin-films, it has also been applied to study the in-plane thermal conductivity of thin-films and axial thermal conductivity of nanowires and nanotubes later. This method provides a sinusoidal current at frequency ω in a metal line to generate modulated electrical heating or temperature oscillation at frequency 2ω. The metal line possesses large temperature coefficient of resistance (TCR), thus its electrical resistance also oscillates at 2ω, further inducing a voltage drop between the ends of the metal line at 3ω. As a result, this 3ω voltage drop and the original 1ω voltage drop can be utilized to calculate cross-plane thermal conductivity of thin film.

Through changing the width of the heating line, the in-plane thermal conductivity of thin film can also be obtained. Choi and coworkers[8, 10] applied 2-pad 3ω and 4-pad 3ω method to investigate thermal conductivity of suspended MWNT; Wang and coworkers[16] explored thermal conductivity of SWNT on substrate through 4-pad 3ω method. However, this method is inconvenient for samples with low or changing thermal coefficient of resistance. Besides, the coupling of electrons and phonons can be quite non-equilibrium in high-quality SWNT electrically charged. Therefore, Pop and coworkers[15, 42] developed a coupled electron-phonon

transport model to account for the non-equilibrium transport in the self-heating SWNT.

1.4.2 SUSPENDED MICRO-THERMOMETER

To avoid heat and charge leaking to the substrate during measurements, different suspended micro-thermometers have been designed. Fujii and coworkers[9] made a T-Junction sensor to investigate the thermal conductivity of individual MWNT. The MWNT bridged a suspended metal film and silicon substrate to form the T shape. Part of the Joule heat of the metal film would transfer to the substrate through the MWNT bridge when the metal film is charged, thus the thermal conductance of the MWNT can be analyzed through this self-heating measurement.

Moreover, Shi and coworkers[12, 40] have developed a suspended platinum resistance thermometer that widely used to determine the in-plane or axial thermal conductivity, Seebeck coefficient, and electrical conductivity of thin films, nanowires and nanotubes. It is composed of two isolated silicon nitride membranes anchored to the substrate through very long and thin beams. Serpentine platinum nanowires are patterned on the membranes and beams to work as heater and sensors. The samples under investigation will be placed across these two membranes, and the thermal properties of the sample can then be analyzed through the temperature changes on the membranes. Later, Wingert and coworkers[43] added a Wheatstone bridge circuit to improve the measurement sensitivity, and applied to samples with much lower thermal

conductivities. Besides, the present work investigating individual SWNTs is based on this method, and details will be explained in the following chapter.

1.4.3 RAMAN SPECTROSCOPY MEASUREMENT

Because of the Raman peak shift with temperature, Raman spectroscopy has been employed to determine the temperature of carbon nanotubes optically[44] or electrically[17, 45] heated, thus the thermal conductance as well as contact thermal resistance can be deduced. However, the temperature sensitivity of the Raman scattering[46] is too low to provide high precision measurements. Moreover, the laser absorption during measurements are ignored, which adds another source of uncertainty. The complexity relating to non-equilibrium transport of various energy carriers limited the capacity of this Raman thermometry technique.

CHAPTER 2 MOTIVATION, CHALLENGES AND ORGANIZATION OF THE THESIS

2.1 MOTIVATION AND CHALLENGES

Since the discovery of CNTs in 1991 by Iijima[29], many potential applications have been suggested and examined[47, 48], such as Hydrogen storage[49], field emission devices[50, 51], nanoscale electronics[52], transistors[53], sensors[54, 55], probes[56, 57], solar cells[58, 59], et cetera. Due to its significant thermal conductivity along the axial direction, its probable prospects in the field of thermal managements has attracted many researchers and engineers, especially as a thermal interface material (TIM)[60-62] to enhance the heat dissipation and cool down the fast-running electronics. The integration of electronic chips keeps on advancing with the development of nanotechnology, which leads to the heat generation per unit area ever higher, the traditional convection cooling method can no longer efficiently alleviate the situation. With SWNTs bridging the hot chips and heat sink, the unwanted heat in electronics can be spread out effectively in order to maintain the stability and longevity of the working devices. In such cases, the axial thermal conductivity of SWNTs deserves careful examination to provide reliable scientific guides for engineering designs.

There has been large amount of experiments conducted concerning the axial thermal conductivity as has been shown in Table 1-1. However, the various CNT preparation methods as well as different measurement methods make the results ranging hugely and hardly comparable with each other. The hidden reason behind this challenge is the difficulty to identify the structure of the SWNTs being studied. Furthermore, the chirality-specific SWNT growth has been

realized[63-65], which have excited the application in electronics[53, 66], then the thermal behaviors of individual SWNT with specific nanoscale structure are more urgently needed to be addressed. Most of the current available experiments have only examined the length and diameter of the CNTs, but the periodic table of SWNTs demonstrates to us that there can be many different SWNTs with the same or very close diameters. Besides, the length of SWNT is another critical parameter that determines the number of phonons in it, but the length dependency of phonon conductance in SWNT is still a controversial debate in theoretical investigations[5, 6], and due to the challenges of sample preparations, there are scarce experimental studies to clarify the disagreement. The unsettlement and insufficiency of the structure dependency of thermal transport properties in SWNTs motivate us to systematically study the relationship of the thermal conductance and its nanoscale structure with the high-quality defect-free horizontally aligned SWNTs. Tackling the structure dependency in individual SWNTs would help us better manipulate its extraordinary thermal properties to serve for future applications.

Except individual SWNTs, the newly developed methods have fabricated high-quality free-standing SWNT thin films[67-69], and they have manifested great properties in optics, mechanics and electronics[70], and these properties are widely studied in comparison with the ignorance of the thermal properties. Moreover, they are expected to be good thermoelectric materials since the inter-tubes interactions hugely impedes the phonon transports but not the electron transports, thus resulting of a lower thermal conductivity as a whole and a higher thermoelectric figure of merits, and exciting *ZT* values from SWNT thin films have been reported

recently[27, 71-73]. However, in comparison with the mature methods to measure the electrical conductivity, the in-plane thermal conductivity of SWNT thin films has not been carefully investigated or even roughly estimated in those reports, which would lead to an overestimation of the *ZT* values. The shortage of available methods to conduct such investigations stimulates us to establish a quick new method with the infrared (IR) thermography to study the macroscale SWNTs film.

Generally speaking, the controversy and disagreement in the thermal transport properties dependency on their atomic structure in nanoscale individual SWNTs or formation structure in microscale SWNT bundles or macroscale thin films elicit our attentions onto them in the present work, in order to provide scientific guidance for future engineering designs and manipulations through the systematic investigations.

2.2 ORGANIZATION OF THE THESIS

This Thesis is aiming to investigate the structure related thermal transport properties in macroscale SWNT thin films by IR measurement as well as nanoscale individual SWNTs by micro thermometer.

At first, information about the SWNTs and previous studies concerning to it have been briefly introduced and reviewed in the first Chapter. This Chapter has provided the motivations,

challenges and organization of the present work. In Chapter Three, a quick and handy method to measure the in-plane sheet thermal conductance of SWNT thin films is proposed with the steady-state IR thermography, and four types of free-standing SWNT thin films are examined by this method, which proves the validity of the new method. In Chapter Four, the suspended micro-thermometer was fabricated and its auxiliary measurement setup was assembled to study the thermal properties of individual SWNTs with the bundle size. At the end, the main merits of this thesis are summarized.

CHAPTER 3 MEASUREMENT OF SHEET THERMAL CONDUCTANCE OF SINGLE WALLED CARBON NANOTUBE THIN FILMS BY STEADY-STATE INFRARED THERMOGRAPHY

3.1 BACKGROUND

Waste heat utilization has attracted worldwide attention due to the pressing energy crisis, hence thermoelectric(TE) materials owe to its simple and direct conversion from low-grade waste heat into high-grade electric power stand out as a promising candidate to ease the severe problem of this century[74, 75]. Of the current commercially available TE materials, the high cost, toxicity, inflexibility, and heavy weight are the obstacles for their broad applications. Therefore, extensive researches have been invested in organic TE materials[27, 71-73, 76, 77] that are cheaper, non-toxic, flexible and lighter, among which CNT thin film shows its great potential[27, 71-73] thanks to its abundance in nature and superb mechanical properties. Although the thermal conductance of individual CNTs are significantly high, the weak van der Waals interactions between nanotubes and the finite length of CNTs in network are expected to hugely suppress the thermal conductance of the thin mats or films[20, 78], while its electrical properties has not been affected much[67, 68]. Contrast to the easiness of obtaining the electrical properties of CNT thin films with well-studied theories and experiments, the thermal properties on the other hand are short of fairly verified methods to account for. To borrow the reported value[72] is misunderstanding, since the reported values can vary in a very large range, due to the diverse preparation methods, from good conductor to fine insulator of CNT films or mats[79], which also exhibit in Table 1-1. Elsewise, with a magnitude thicker supporting substrate[27, 73], parasitic heat loss to the substrate makes the measured thermal conductance be far away from the true heat transfer capability of the thin film under investigation, so does the local heaters or

thermometers in contact. Therefore, substrate-free and contact-free methods are most ideally preferred.

3.2 MOTIVATION AND SCOPE OF THE PRESENT WORK

The current techniques that avoid substrate and contact include Raman spectroscopy measurement which has made a success to determine the superior thermal conductance of graphene sheet[80, 81], whereas the imperative and intricate calibration limits its application to more materials. The four-probe measurement on suspended resistance thermometer micro devices[12] is also frequently adopted, thanks to its regardless of the material types [82, 83] and free of calibration, but the demanding sample preparation procedures restrict the broader prospect, as the complex procedure indicating in the last chapter. Another alternative would be ultrafast thermo-reflectance[84], yet the calibration and smooth surfaces without diffuse reflection are also challenging. Otherwise, infrared (IR) thermography is a straight and quick method to record the temperature profiles of the targets, along with some ad hoc designing to calculate the heat flux, it can develop into a direct and handy technique for contactless thermal conductance determination[24, 85].

In this chapter, a steady-state IR thermography measurement was established to investigate the in-plane sheet thermal conductance of four SWNT thin films, with transparency of 60%, 70%, 80% and 90% respectively. The thin films are suspended in between the free ends

of two cantilevered silicon thin plates, with a steady-state heat flux flowing along silicon-SWNTs-silicon then generating a constant temperature gradient which is recorded by the IR camera. The silicon plate with known thermal conductivity is the reference to calculate the constant heat flux, furthering to obtain the sheet thermal conductance of SWNT thin films through Fourier's law after deducting the influence from thermal radiation. This novel but simple method can extend to any other free-standing thin films.

3.3 EXPERIMENT DESIGN

The principle of the experiment is to provide a substrate and contact-free method to measure the thermal conductance of the free-standing SWNT thin films.

3.3.1 EXPERIMENTAL SETUP

To measure the thermal conductance, a temperature gradient should be generated in the material under investigation with a known heat flux. Experimental setup in the present work is arranged to form a quasi-one-dimensional steady-state heat transportation. Shown in Figure 3-1(b) is the exploded view of the measurement setup. A copper heater is placed in the cavity of the insulator cuboid and covered with aluminum plate; on the other side, parallel to it is a bulk copper. These are the heat source and heat sink, respectively; then two pairs of silicon plates (with width of 3mm or 2mm and thickness of 100μm) covered with black paint on their surfaces

are aligned with each other on heat source and sink. SWNT thin film is dry transferred to suspend in between the free ends of one pair of aligned silicon cantilevers. Four thermal couples are attached with Kapton tape on the surfaces of the silicon plates at the verge of heat source or sink, which are in the view of the IR camera, to calibrate the emissivity of the silicon. Moreover, the whole system is kept in a vacuum aluminum chamber with a ZnSe window (with diameter of 25mm) which barely impede the infrared radiation. Below the chamber is a cooler, to keep the aluminum chamber and the cuboid copper heat sink fixed within it at a constant lower temperature, while an outsider controller provides power to have the heater at a constant higher temperature. Therefore, a steady-state quasi-one-dimensional heat transportation is established along the silicon-SWNTs-silicon bridge after a while. Since the measurement is performed under vacuum, the heat convection can be ignored, while the control experiment without free-standing SWNT thin films and the other unloaded pair of silicon cantilevers are designed to eliminate the influence of thermal radiation and IR camera fluctuation in later calculation, respectively.

The IR camera records the thermal changes of samples from above through the ZnSe window; shown in Figure 3-1(a) is the temperature profile of the quasi-one-dimensional steady-state heat transfer with SWNT thin film of 60% transparency. In between the heat source and heat sink is the real-time thermal image taken by the IR camera, and beside the schematic heat sink is the legend of IR thermography. The temperature on the higher temperature silicon plate is out of the current display range in order to clearly show the temperature gradient on SWNT thin film and that on the lower temperature silicon plate which is the reference to calculate the

heat flux through the mixed bridge. However, the temperature on the SWNT thin film is not real since the emissivity of this image is set at 0.94, which will calibrate in the following part. The IR camera in performance is Avio H2640, high resolution (0.03°C) infrared thermal imaging camera with a 25μm close-up lens, which make the minimum detectable size 25μm by 25μm, with the resolution of 640 by 480 pixels giving a 16mm by 12mm scan range, and the working distance is 11mm. Besides, it detects IR signals in the wavelength range from 8μm to 14μm.

The samples in this study are high quality SWNT thin films, which are prepared by aerosol CVD synthesis method[67]. The SWNT thin films are collected on low-adhesion filters, thus they can be easily transferred to practically any substrate, such as flexible polymers, glass, quartz, silicon and various metals. Therefore, it is not surprising that we successfully dry transfer them to suspend in between the free ends of two silicon cantilevers.

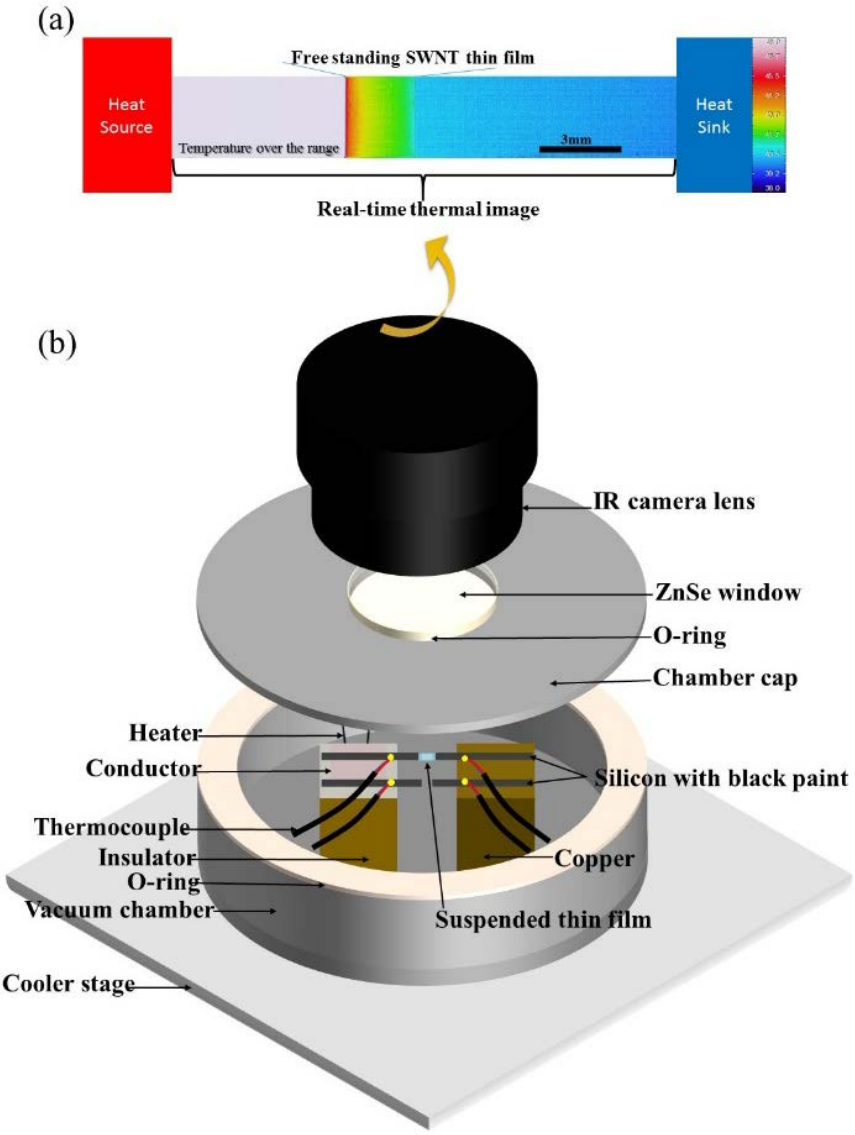

FIG. 3-1 (a) The temperature profile of the quasi-one-dimensional steady-state heat transfer. In between the heat source and heat sink is the real-time thermal image taken by the IR camera, and the legend of the thermography is placed beside the schematic heat sink. The temperature on the higher-temperature silicon plate is out of the current display range in order to clearly show the temperature gradient on SWNT thin film and lower-temperature silicon plate. The SWNT in this image is of 60% transparency, the temperature of the SWNT is not real since the emissivity of the image is set at 0.94; (b) Exploded view of the measurement setup.

3.3.2 TEMPERATURE MEASUREMENT

The cantilevered silicon plates, which is the critical part to calculate the heat flux, are covered with black paint of emissivity around 0.94, and we calibrate the IR camera through comparing the temperature in the thermal image with that of the thermal couples in the same area on the anchored part of the silicon plate at different temperatures, then the IR image taken at the adjusted emissivity reflected the true temperature on the silicon. However, the IR image then cannot tell the true temperature of the suspended SWNT thin film since its emissivity is much lower. Via FT-IR we measure the absorbance of the four SWNT thin films, shown in Figure 3-2, which indicates that the emissivity of the four highly transparent thin films can be as low as less than 0.1 because Kirchhoff's law states the emissivity equals the absorptivity when the surface of the object can be approximated as a gray body. The adjustable emissivity of the IR camera is from 0.1 to 1, thus we need some extra calibrations to obtain the temperature distribution on the suspended thin films.

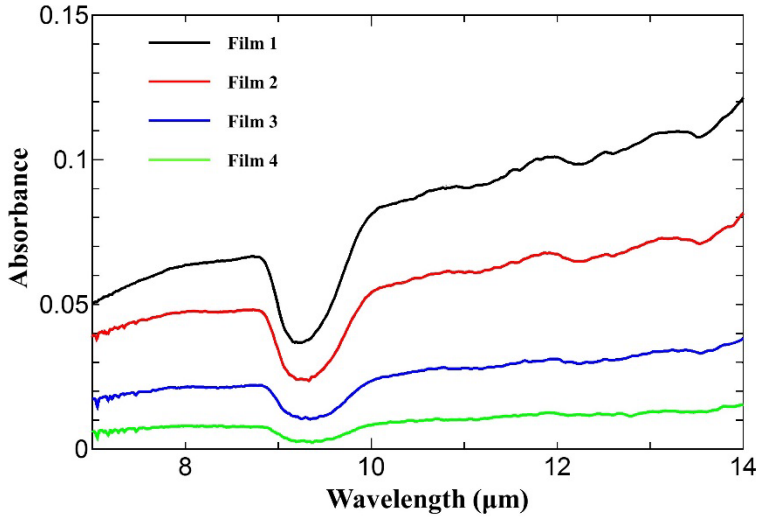

FIG. 3-2 Absorbance taken by FT-IR of the four types SWNT thin film, film 1 to 4 corresponding to SWNT thin film with transparency of 60%, 70%, 80% and 90%.

The object temperature is determined in the IR camera as follows[86]:

$$T_{obj} = \left\{\frac{1}{\varepsilon}\left[\frac{1}{\tau_a}T_r^n - (1-\alpha)T_u^n - \frac{\varepsilon_a}{\tau_a}T_a^n\right]\right\}^{1/n} \quad \text{Eq. (3-1)}$$

where ε_a and τ_a are the emissivity and transmission of the air respectively and $\varepsilon_a = 1 - \tau_a$, while ε and τ are the counterparts of the object under investigation; T_{obj}, T_r, T_u, T_a are the temperature of the object, the radiative temperature of the object, the environmental temperature and the atmospheric temperature, respectively. Since the measurements are performed in a very short distance, the effect of atmospheric absorption can be ignored, then $\tau_a = 1$, thus the above equation can be simplified to α_a

$$T_{obj} = \left\{\frac{1}{\varepsilon}[T_r^n - (1-\varepsilon)T_u^n]\right\}^{1/n} \quad \text{Eq. (3-2)}$$

Because the infrared thermometers only covers particular range of the wavelength and the exponent n depends on the wavelength, $n = 4.09$ is suggested for the sensor of HgCdTe (8~14μm) in use from reference[87].

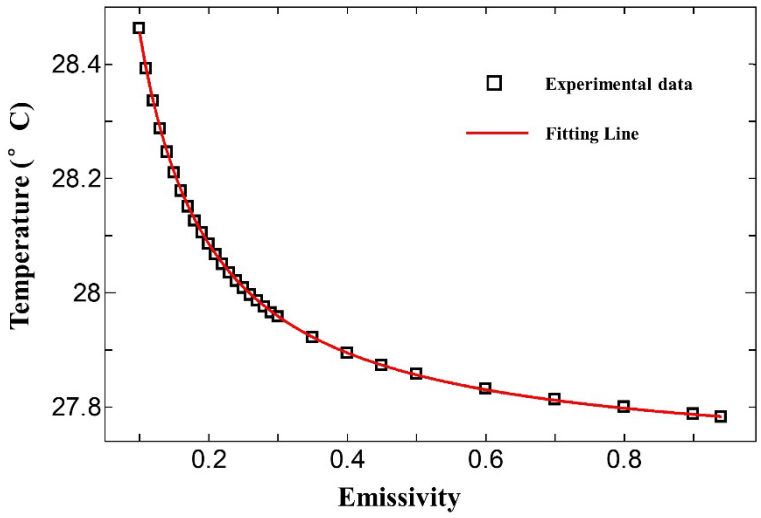

FIG. 3-3 Fitting the temperature vs. emissivity with Eq. (4-2) to extrapolate the true temperature distribution in the suspended SWNT thin film.

IR images at different emissivity are taken in order to calculate the temperature on the SWNT thin film. With the temperature T_{obj} read by IR camera at different ε, the data are fitted with the above Eq. (3-2) thus the T_r and T_u can be obtained as the fitting parameters for the sample under investigation, as shown in Figure 3-3. With the certainty of T_r and T_u, the temperature of the SWNT thin films with emissivity out of the range of the current IR camera can be determined, thus the temperature distribution of the suspended thin films is acquired. The temperature points on *y* axis at the same *x* point are averaged to obtain the quasi-one-dimensional temperature distribution along the silicon-SWNT-silicon bridge, as demonstrated in Figure 3-4. The very verge of the suspended thin film is blurred due to the focus of the IR camera, so the temperature distribution is not continual at those points after they have been neglected. The wrinkles caused during dry transfer lead to some local congestion of thin films, which generates

the non-uniformity of the temperature points in SWNT thin film in consequence, shown by the green points in Figure 3-4. Apart from that, the linear temperature profile in the suspended SWNT thin film is verified, which proves the validity of this method. Therefore, the temperature of the silicon at the contacts can be taken as the temperature of the thin film at that points to calculate the temperature drop in the suspended SWNT thin films, since the films and contacts are in macro-scale where the contact resistance can be left out of consideration.

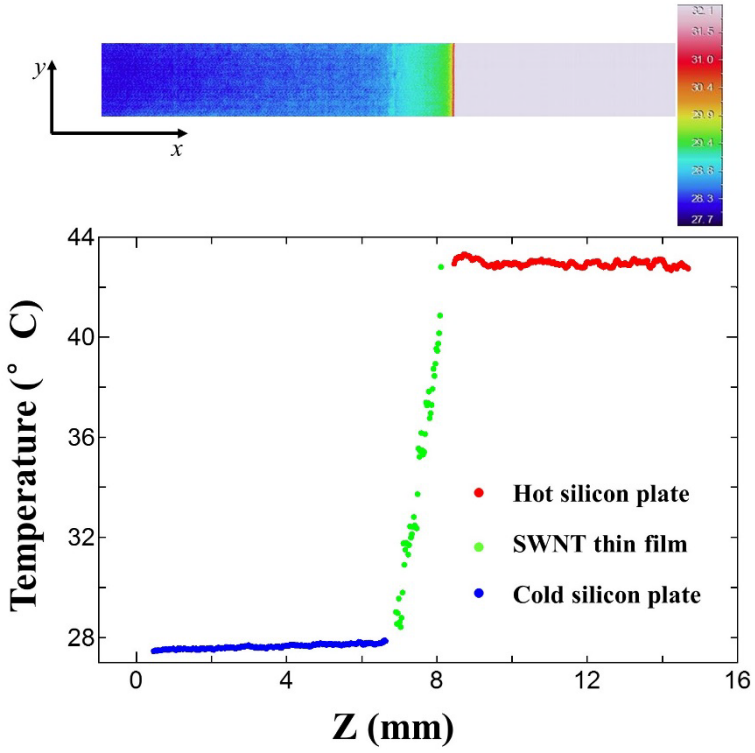

FIG. 3-4 The quasi-one-dimensional temperature distribution along the silicon-SWNT-silicon bridge with SWNT thin film of 80% transparency.

3.3.3 UNCERTAINTY ANALYSIS

The unloaded parallel silicon pair helps to eliminate the influence from the noise of the IR camera, and the control experiment without film provides a method to deduct the background radiation noises. The random uncertainty from averaging the ten data sets and fittings are transferred to the calculation of sheet thermal conductance by the same way as specified in the last chapter, and are incorporated in the error bar in Figure 3-7.

3.3.4 NOISES AND SENSITIVITY

The radiant heat transfer is the largest noise in this experiment, and it can be approximated as

$$G_{rad} = A_1 \sigma \varepsilon_1 F_{12} (T_1^2 + T_2^2)(T_1 + T_2) \qquad \text{Eq. (3-3)}$$

here, A_1 is the cross-sectional area of the copper; F_{12} is the view factor from heater to sink, which is about 0.5; σ, the Stefan-Boltzmann constant; ε_1 is the emissivity of the heater surface, about 0.2; thus G_{rad}, the thermal conductance of the radiation, is on the order of 10^{-6} W/K by the above definition. Therefore, a control experiment is necessary to rectify the measurements.

The cantilevered silicon on the low-temperature heat bath is chosen as the reference to calculate the conduction heat flux through the suspended SWNT thin film because of the less radiation disturbance. Apart from the radiation, the fluctuation of the IR camera also causes an observable noise to the system. To decrease and calibrate the noises, another cantilevered silicon pair unloaded (shown in Figure 3-1(b)) is placed side by side with the silicon-SWNT-silicon.

Thus, the difference of temperature gradients on the two lower-temperature silicon plates is free of the perturbation from the IR camera. The experiment in the same condition is repeated without the SWNT thin film in order to deduct the influence from thermal radiation in later calculation. In addition, the thermography takes ten images every experiment and then averaged to obtain the temperature distribution in due experiment, the schematic temperature profile is indicated in Figure 3-5.

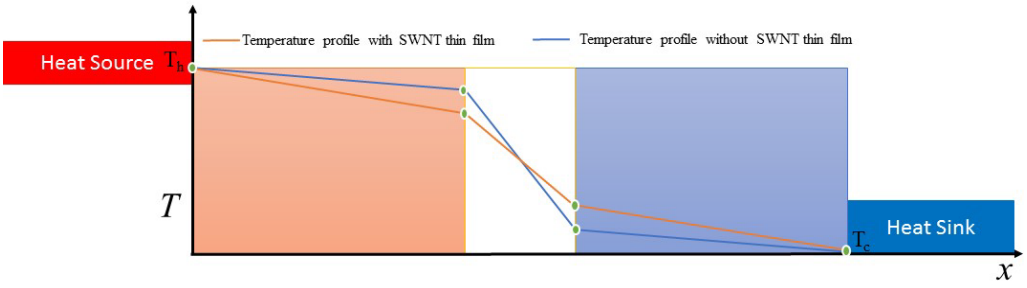

FIG. 3-5 Schematic temperature profiles along the silicon-SWNT-silicon bridge with and without SWNT thin film to calculate the heat flux through suspended thin film.

The resolution of the IR camera is 0.03°C, then the minimum observable temperature difference on silicon plate *dT* is 0.03K. Taking this value into Eq. (3-6) below, the smallest sheet thermal conductance can be measured by this method will be $\frac{\lambda_{Si}\times 0.03\times \Delta x_{SWNT\ thin\ fillm}\times t_{Si}}{dx\times \Delta T_{SWNT\ thin\ film}}$, the length of the cantilevered silicon plate *dx* is thrice of the suspended length of SWNT thin films *Δx* in our experiment design, and the thickness of the silicon plate is 100μm, therefore, the minimum detectable sheet thermal conductance is determined by

$$\frac{\lambda_{Si}}{\Delta T_{SWNT\ thin\ film}} \times 10^3 \qquad \text{(nW/(K□))} \qquad \text{Eq. (3-4)}$$

This equation reveals that the larger the temperature difference Δ*T* in SWNT thin film, the

smaller the detectable sheet thermal conductance by the present method, which means the higher sensitivity. However, the larger temperature difference will bring the noisier radiation disturbance which will degenerate the correctness on the other hand. With the same temperature difference between heat source and sink in all of the four experiments with SWNT thin films of different transparency, these two contradictory factors lead to the largest measurement uncertainty for the lowest sheet thermal conductance film, but since the radiation effect will be deducted through control experiment, this is not a concern. The heat source of 60°C and heat sink of 15°C in the experiments have been set after a lot trials resulting a sensitivity on the order of 10^{-6} W/K, which implies the non-negligibility of the radiation in the experiments.

3.4 EXPERIMENTAL RESULTS AND DISCUSSIONS

One dimensional steady-state heat transport by conduction as illustrated in Figure 3-5 tells,

$$Q_{cooler\ silicon} = Q_{SWNT\ thin\ film} \qquad \text{Eq. (3-5)}$$

Taking Fourier's Law into Eq. (4-5), the following equation is satisfied.

$$\lambda_{Si} \times \left[\left(\frac{dT}{dx}\right)_{cooler\ silicon\ with\ SWNT\ thin\ film} - \left(\frac{dT}{dx}\right)_{cooler\ silicon\ without\ SWNT\ thin\ film}\right] \times t_{Si} \times W_{Si} = \lambda_{SWNT\ thin\ film} \times \left(\frac{\Delta T}{\Delta x}\right)_{SWNT\ thin\ film} \times t_{SWNT\ thin\ film} \times W_{SWNT\ thin\ film} \qquad \text{Eq. (3-6)}$$

In Eq. (3-5), λ, t, W are the thermal conductivity, thickness and width of the material denoted in the subscript respectively. The width of the silicon plate and SWNT thin film are the same,

furthermore, thermal conductivity of the silicon plate are available from literature[88] and its thickness is 100μm. The temperature gradient on silicon plate and SWNT thin film can be calculated from thermography according to the analyses of last section. Then, there remains the product of thermal conductivity and thickness of SWNT thin film to be determined. The thickness of SWNT thin film are not easy to be certain, which is proportional to its transparency or the growth time and is changeable in different conditions[67]. Therefore, we decide to treat the product as a new term and call it sheet thermal conductance.

3.4.1 SHEET THERMAL CONDUCTANCE

The sheet thermal conductance is coined analogous to the sheet resistance. Eq. (3-7) is the deduction of sheet resistance, of which R is the electrical resistance, σ is the resistivity, A, L, W and t are the section area, length, width and thickness of the material respectively, R_S is the sheet resistance and its unit is Ω/□. The electrical conductance G_e is the reverse of electrical resistance, so Eq. (3-7) can be equally expressed by Eq. (3-8). Accordingly, the thermal conductance G_t is the product of the thermal conductivity λ multiplies the cross-sectional area A then divide the length L; then the cross-sectional area A can be split into the width W and sheet thickness t. Upon combining the film thickness with the thermal conductivity, the thermal conductance can be written as the second column in Eq. (3-9), where the G_{st} is the new term, sheet thermal conductance. If the film thickness is known, the bulk thermal conductivity is the quotient of the sheet thermal conductance over its film thickness. Sheet thermal conductance is

a special case of conductivity for materials with a uniform sheet thickness and the SWNT thin films investigated in this work are just as such. Like the unit Ω/□ is used exclusively for the sheet resistance, W/(K□) is suggested to be the unit of the sheet thermal conductance. This new term is a good description of the heat transfer capability for thin films that regardless of thickness. For the 2D materials or thin film with a nanoscale thickness, the cross-sectional area is hard to define or measure. In these cases, the sheet thermal conductance can provide a comparable evaluation of heat transfer.

$$R = \frac{L}{\sigma A} = \frac{L}{\sigma W t} \;;\; R = \frac{1}{\sigma t}\frac{L}{W} = R_s \frac{L}{W};\; \sigma = 1/R_s \cdot t \quad (\Omega/\square) \qquad \text{Eq. (3-7)}$$

$$G_e = \frac{1}{R} = \sigma \frac{A}{L} = \sigma \frac{Wt}{L};\; G_e = \sigma t \frac{W}{L} = G_{se}\frac{W}{L};\; G_{se} = \sigma t \qquad \text{Eq. (3-8)}$$

$$G_t = \lambda \frac{A}{L} = \lambda \frac{Wt}{L};\; G_t = \lambda t \frac{W}{L} = G_{st}\frac{W}{L};\; \lambda = G_{st}/t \quad (\mathrm{W}/(K\square)) \qquad \text{Eq. (3-9)}$$

Four types free-standing SWNT thin films with different transparency, which are 60%, 70%, 80% and 90% respectively, are examined in this study. The upper four pictures in Figure 3-6 shows the optical images of these four thin films which shows that the films are getting lighter with increasing transparency from left to right. In addition, the below two pictures of Figure 3-6 are the SEM image of SWNT thin film with transparency of 80% and the TEM image of the film with 90% transparency respectively, which suggests that the thin films are composed of high-quality, very long SWNTs. Besides, the SWNT bundles sizes are quite small in the thin film, suggested by the TEM image, including even many parts of isolated SWNT and two- or three-SWNT bundles.

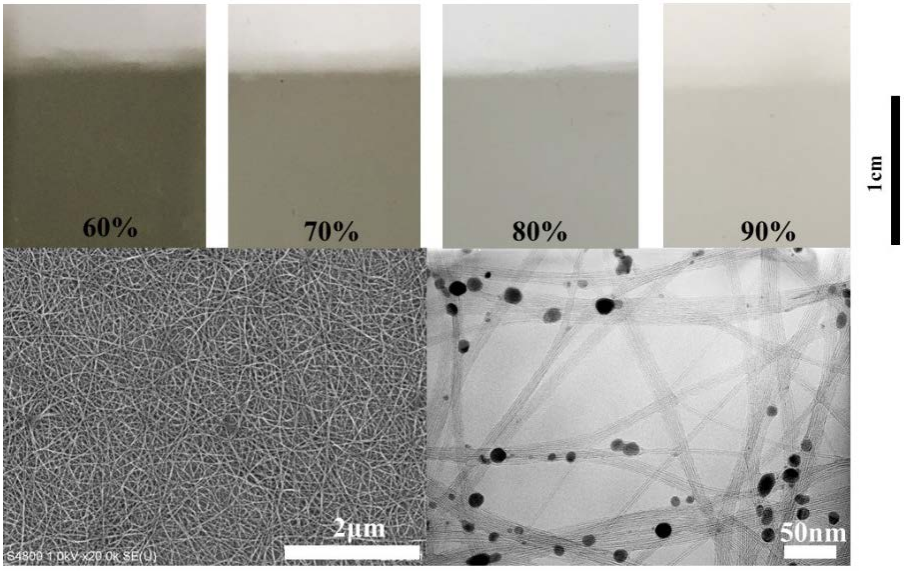

FIG. 3-6 The upper four pictures are the four SWNT thin films with transparency of 60%, 70%, 80% and 90% from left to right respectively, the light color on the very top is of the filter paper, the sale bar on the very right for them is 1cm; the left below picture is the SEM image of SWNT thin film with transparency of 80% and the right one below is the TEM image of SWNT thin film with transparency of 90%.

3.4.2 THERMAL CONDUCTIVITY

The relationship of sheet thermal conductance and transparency is plotted in Figure 3-7. The sheet thermal conductance is decreasing with the increasing transparency due to the decreasing film thickness of higher transparency. However, the increase is not linear. The reason might lay to the non-linear proportion of transparency to the film thickness. Besides, from the TEM image in Figure 3-6, it exhibits that the density of SWNT thin film fundamentally is not uniform, that is to say the number of the SWNTs is not necessarily a linearity to the thickness, while the heat transfer capability of the sheet is the net effect of the individual SWNTs, hence,

there is no guarantee that the sheet thermal conductance should increase linearly with the thickness or the transparency.

Except the IR measurement, Raman spectroscopy was also conducted to explore the thermal properties of the same four SWNT thin films[89], which was denoted by the red dots in Figure 3-7. The trend of the results by Raman measurement is the same as the IR measurements, but the values are 1.9 to 2.5 times lower. Contrary to the well-accepted assumption that near thermal equilibrium are realized between different phonon polarizations in Raman measurements, a first-principle study with monolayer graphene has revealed that strong nonequilibrium are popular in electrons, optical phonons and acoustic phonons, which would result in an underestimation of thermal conductivity in experiments by a factor of 1.35-2.6 at room temperature due to the conditions of the Raman measurements[90], in which the flexural acoustic, the main heat carrier in suspended graphene[91], shows the largest nonequilibrium. The flexural acoustic phonons are also major contributors to the high thermal conductivity[92] in SWNT, and the non-equilibrium between different phonon polarizations are expected[93]. Therefore, this nonequilibrium in Raman measurement might be the main reason of the difference from the thermal conductivities of SWNT thin films determined by IR measurements.

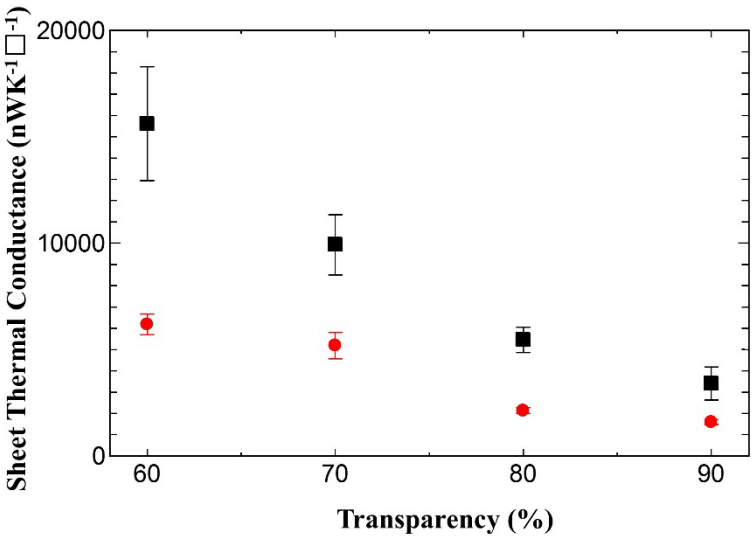

FIG. 3-7 Sheet thermal conductance of the four SWNT thin films measured in this work are denoted by the black squares, from left to right is corresponding to the thin films with transparency of 60%, 70%, 80% and 90%; the red dots were measured by the Raman measurements[89] with the same SWNT thin films.

AFM and optical interference are adopted to estimate the thickness of the 90% transparency film to be around 50nm[67]. By the definition of sheet thermal conductance in Eq. (3-4), the thermal conductivity of this film can be calculated to be around 68.1$Wm^{-1}K^{-1}$. This value is higher than the previously measured multi-walled random CNT films and most of the sorted multi-walled CNT films[79], but it is reasonable because the thin films in this study are composed of high-quality and very long SWNT[67, 94], as shown in Figure 3-6, meanwhile single SWNT possesses very high thermal conductivity[2, 14] and it is increasing with the length of SWNT[3, 95]. Furthermore, the intrinsic thermal conductivity of SWNT in the network has a great contribution to the overall thermal conductance of the thin films[78]. In comparison with other measurements[22, 27] which show much lower thermal conductivity of carbon nanotube

thin films, the TEM images suggest that the bundles sizes of the thin films in this study is smaller, which have been expected to contribute the most to decrease the thermal conductivity of bulk carbon nanotube thin films[20]. Therefore, the less bundled SWNTs in the thin films of this study might be another main contributor to the high thermal conductivity.

3.5 CONCLUSIONS

In summary, a quick and non-contact method for the measurement of in-plane sheet thermal conductance of SWNT thin films with the steady-state infrared thermography have been presented here. The SWNT thin films are free-standing in between two cantilevered silicon thin plates which work as the reference to calculate the heat flux through SWNT thin film. The temperature profile along the silicon-SWNT-silicon bridge is recorded with the IR camera. Besides, another unloaded parallel silicon pair is set in order to offset the noise from the camera. A control experiment without film is also conducted to account for thermal radiation. Since the thickness of SWNT thin film in this study is hard to determine and it is changeable under different conditions, sheet thermal conductance is proposed to evaluate the capability of heat transfer of SWNT thin films.

The results indicate the sheet thermal conductance are 15613.4±2672.5nW/K, 9925.4 ±1417.1nW/K, 5454.8±594.9nW/K and 3405.7±773.8nW/K at room temperature for SWNT thin films with transparency of 60%, 70%, 80% and 90%, respectively. Therefore, for the 50nm

SWNT thin film of 90% transparency, its thermal conductivity is around 68.1$Wm^{-1}K^{-1}$, which is benefitting from the composition of the high-quality and very long SWNTs by aerosol CVD synthesis method as well as the less bundled SWNTs. The sensitivity of This method is no the order of 10^{-6} W/K and can be applied to any other films (especially low thermal conductance films) that can be transferred to free-standing in between the cantilevered silicon pair plates.

In comparison with the Raman measurements of the same SWNT thin films, the strong non-equilibrium of different phonon polarizations and electrons might contribute to the lower thermal conductivity by a factor of 1.9-2.5 in our cases. The relatively higher thermal conductivity of the SWNT thin films in this study suggests that the smaller bundles sizes in composition might refrain the thermal transport properties from further degradation.

CHAPTER 4 INVESTIGATION OF THERMAL TRANSPORT PROPERTIES OF INDIVIDUAL SINGLE WALLED CARBON NANOTUBES BY MICRO-THERMOMETER COMPATIBLE WITH TEM

4.1 BACKGROUND

The one-dimensional quantum effect participated the unique electronic properties of carbon nanotubes[96], which firstly promoted the studies on carbon nanotubes. The potential applications in the future making the best of the extraordinary not only electronic, but also mechanical, optical, thermal characteristics further attracted the focus in academic societies. Two years after the discovery of MWNT[29], SWNT comes into the view of humans[30]. Even before its synthesis, many theoretical studies were conducted with SWNT, because of the much fundamental base of its existence. In 1996, Smalley and his group synthesized the CNT arrays[97], which was a huge breakthrough in the studies of CNTs and directly brought the investigation of SWNT from theoretical area to experimental field. Afterwards, many other synthesis methods[31, 32, 98-100] were materialized and mass production of CNTs has been realized for academic studies or industrial trials, which provided the chance to experimentally examine the theoretically predicted super-high axial phonon thermal transport in CNTs and the prospects in thermal management.

With the further development of miniaturization in electronics, heat dissipation in micro/nano scale has bothered engineers. Even though the miniaturization of electronic devices has decreased the supplication of energy, the rapid increase of energy density is unavoidable, which makes the effectiveness, stability and longevity of devices in performance highly dependent on the thermal transport efficiency of materials. Moreover, the extra heat has limited

the further miniaturization, thus new materials for electronics also with superb thermal properties are strongly needed to ease this dilemma. Nanoscale SWNT with symmetrical structure shows remarkable electrical characteristics as well as thermal properties in its axial direction, promoting itself to be an upstart in this needy field. However, the present available researches are confined by the precise structure identification of individual SWNT, resulting of the large variant estimations of its capability in heat transferring, as having been indicated in Table 1-1.

4.2 MOTIVATION AND SCOPE OF THE PRESENT WORK

Many molecular dynamics simulations have been conducted regarding to structure dependent thermal transport properties of CNT, as summarized in Table 4-1, but the experimental investigations are fewer in comparison. In addition, the existing experimental investigations are under no condition to be compared for analyzing, due to the blindness of the specific structure of the studied CNTs. This shortage motivates the present work focus on the investigation of the thermal transport properties of individual SWNTs with structure specification.

Up to date, only one experimental study of thermal transport properties has ever identified the precise atomic structure of one SWNT through transmission electron microscope (TEM)[101]. To systematically study and understand the fundamental thermal behavior of SWNTs, the determination of the nanoscale structure of SWNTs is necessary, which would provide valuable scientific guidance for the design of nanoscale CNT electronics[52, 53, 66].

The length dependent thermal conductivity of SWNTs are theoretically studied in many literatures due to the interest of confined phonons, but the results are inconclusive and controversial. Some concluded that the thermal conductivity of SWNTs will converge with the increasing length due to the transition from ballistic to diffusive phonon transport, while others suggested that the thermal conductivity of SWNTs would keep increasing since the quasi-one-dimensional structure can hold very long phonons. The only available experimental study[26] claims that the thermal conductivity keeps increasing even to 1mm. As to the thermal transport dependency on chirality, the previous simulation results are also in conflicts and disagreements, as implied in Table 4-1.

Table 4-1 Molecular dynamics simulation summary: the length *L* and thermal conductivity *κ* are the convergence values when *κ* converges with length or the largest values in the study if not. The values are corrected with the cross-sectional area of the nanotube defined as $A=\pi D\delta$, δ=0.34nm is the thickness of graphene sheet.

Length dependency				
Chirality	*L* (nm)	*D* (nm)	*κ* ($Wm^{-1}K^{-1}$)	Convergence or Divergence
(10, 10)	40	1.36	876	Convergence[102]
(5, 5)	404	0.68	550	Divergence[3]
(10, 10)	150	1.36	350	Convergence[103]
(10, 10) (18, 0) (14, 6)	9.908 8.580 15.252	1.36 1.40 1.38	890 815 780	Convergence[104]
(5, 5) (10,10)	100 100	0.68 1.36	1480 1160	Divergence[105]
(10, 10)	40	1.36	160	Divergence[7]
(3, 3) (5, 5)	800 1500	0.40 1.36	820 640	Divergence[106]

Chirality dependency				
Chirality	*L* (nm)	*D* (nm)	κ ($Wm^{-1}K^{-1}$)	
(10, 10) (18, 0) (14, 6)	9.908 8.580 15.252	1.36 1.40 1.38	1780 1620 1560	Armchair>Zigzag>Chiral[104] Converged values
(9, 0) (5, 5)	Not indicated	0.71 0.68	352 384	No significant reliance[105]
0°~30° (Chiral angle)	20 50 100	0.92 1.64 3.30	100~440	Armchair>Zigzag; Chiral with larger angles>chiral with smaller angles[107]
(20, 0) (11, 11) (10, 13)	2.510 2.899 2.786	1.54 1.46 1.54	7800 3500 1000	Zigzag>Armchair>Chiral[108]

Moreover, as last chapter have suggested the bundle sizes might contribute a lot to the overall thermal conductivity of the bulk thin films, therefore, bundle sizes dependency of the thermal conductivity in SWNT is also intriguing to be addressed. No less than graphite has a much lower thermal conductivity in comparison with its unit cell graphene due to the inter planar interactions, the increased bundles sizes have been expected and experimentally observed to degrade the thermal conductivity due to the interactions between SWNTs[12, 14]. However, because of the difficulty of sample preparation, there is no quantitative study about the relationship of the thermal conductivity of SWNTs and the bundle sizes. In this Chapter, with the transferred horizontally aligned SWNTs which is in uniform conditions, the bundle size can be selectively chosen to realize the quantitative study for the first time.

4.3 EXPERIMENT DESIGN

To study the thermal properties of individual SWNTs, the suspended platinum (Pt) resistance thermometer was fabricated in the present work. The device was first invented by Shi and coworker[12], and later applied to measure thermal properties of nanowires[43, 109, 110], nanoribbons[82] and nanotubes[19, 111] with high sensitivity. The micro-thermometer is composed of two 25μm by 40μm adjacent thermally isolated silicon nitride (Si_3N_4) membranes (one denoted as sensing membrane and the other as heating membrane) anchored to the substrate with four 2μm wide and 450μm long Si_3N_4 beams, as illustrated in Figure 4-1 and Figure 4-2. The thin Pt serpentine lines with width of 400nm and thickness of 38nm are patterned on the Si_3N_4 membranes as the sensor and heater benefiting from its high temperature coefficient of resistance (TCR), and in connection with four Pt leads for four-probe measurement of the resistance of the serpentine lines on the suspended Si_3N_4 beams. At the end of the Pt leads are Pt pads for wire bonding on the substrate, as specified in Figure 4-2. The silicon wafer underneath the suspended structure will be etched completely for TEM characterization of the samples. The horizontally aligned SWNT of high-quality and defect-free[112] will be transferred in between the sensing and heating membranes later. The fabrication processes of the micro thermometer and the SWNT transfer technique will be introduced in details below.

4.3.1 MICRO THERMOMETER DEVICE FABRICATION

The fabrication procedure of the suspended micro thermometer includes two Electron Beam (E-Beam) Lithography (EBL), one Photo-Lithography (PL), two Reactive Ion Etching

(RIE) and one Deep Reactive Ion Etching (DRIE) and many other processes, which are specifically demonstrated and explained in Figure 4-1 and the following paragraphs.

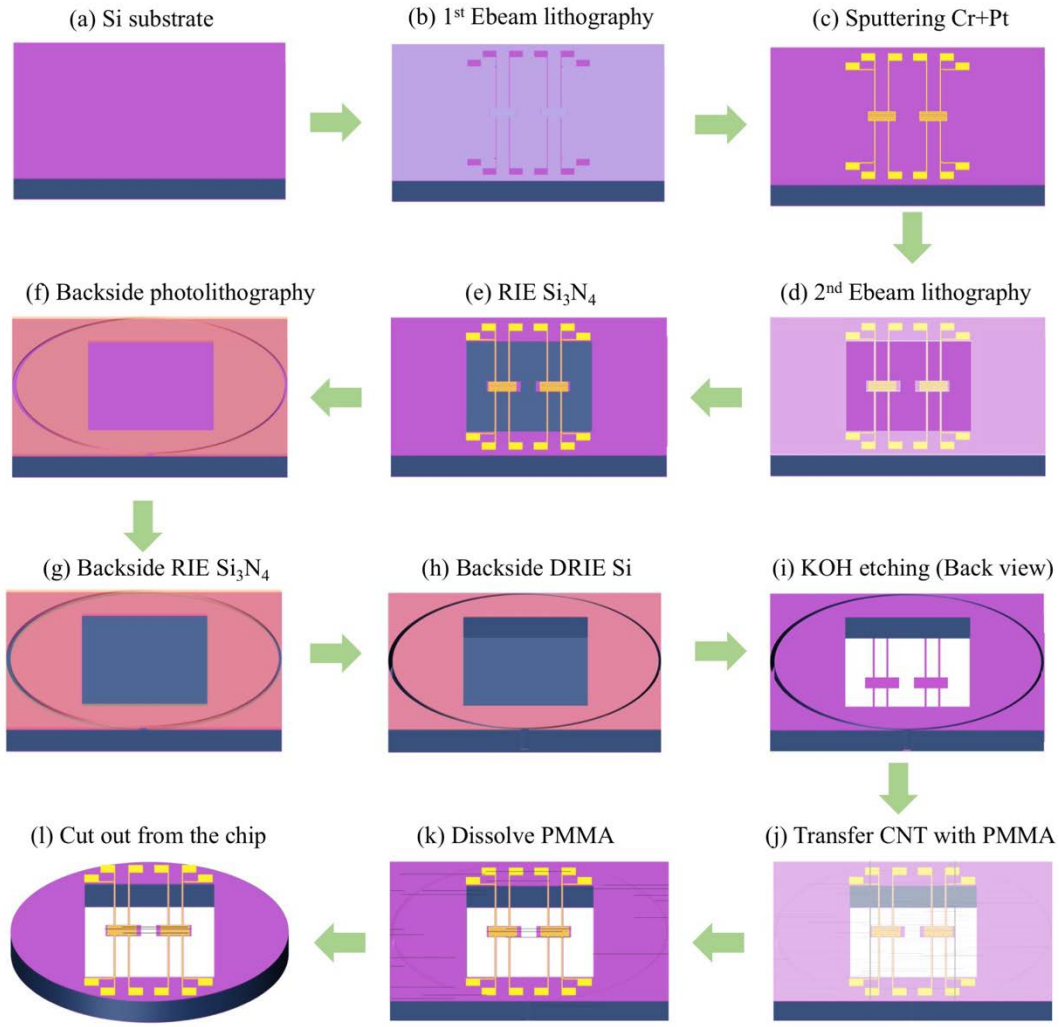

FIG. 4-1 The fabrication processes of the micro-thermometer device, a brief explanation is inserted above the schematic figures: the chip has gone through in sequence ten steps, a EBL to pattern the electrodes, metal deposition, the second EBL to pattern the suspended features, RIE, Backside photolithography to open the window, RIE again, DRIE, KOH etching, CNT+PMMA transfer, PMMA dissolving.

The measurement device is batch-fabricated on a 4-inch silicon wafer with 300nm less stressed silicon nitride (Si_3N_4) thin layer on both sides through micro-fabrication technology.

a) Firstly, the wafer is cut into 1-inch square chips with dicing saw.
b) ZEP 520A is spin-coated on the chip with 4000rpm for 60s, which will result with a thickness around 400nm as the first E-Beam resist, the EBL with dose of 106μC/cm^2 is conducted to make the patterns for electrodes, leads and serpentine coils. After developed in ZED-N50 for 60s, a 5s oxygen plasma is followed to further remove some residues in the opening trenches.
c) 2nm Cr and 30nm Pt are then deposited as heating and sensing components by RF sputter, afterwards the chips are immersed in stripper solution (60%DMSO plus 40%NMP) to dissolve remaining ZEP 520A. After the following sonication of several minutes, the heating and sensing metal features are surfaced on the chips.
d) The second layer EBL is followed to make the patterns for the suspended Si_3N_4 pads and beams. OEBR-CAP 112 PM is spin-coated as E-Beam resist at 2500rpm for 60s of about 1.5μm thick, and exposed to E-Beam of dose of 6μC/cm^2. Thus, the suspending characters are materialized after developing in THAM for 60s.
e) Next, RIE is performed with CHF_3 gas to transfer the suspending features from the E-Beam resist to Si_3N_4 thin layer. Later, the chips are annealed at 550°C in the air to decompose the remaining OEBR-CAP 112 PM.
f) To final release and protect the fragile suspended structures on the front, a deep reactive

ion etching (DRIE) window for the suspended micro thermometer alongside with the 3mm circle compatible to TEM characterization are patterned by photolithography from the backside of the chip. AZ P4620 is spin-coated at 3000rmp for 60s, which is around 7.1μm thick, then exposed to ultra violet light for 45s, and developed in THAM for three minutes.

g) With the thick photoresist protecting other parts, the uncovered Si_3N_4 area is etched by CHF_3 in RIE to expose the below 525μm silicon substrate.

h) Then the exposed silicon substrate is fast etched away by SF_6 and C_4F_8 until only a few tens of micrometer remained to support the front micro structures during later treatments.

i) After removing the photoresist, the remaining silicon in the window and circle is completely etched away by 1mol/L KOH solution to ultimately suspend the Si_3N_4 pads and beams with heating and sensing serpentine Pt coils and leads. By now, the whole device is complete and the optical images of a typical micro thermometer device is shown in Figure 4-2.

j) When the SWNT sample preparation is ready, which will explain in details in the later part, it will be transferred with PMMA onto the chip across micro thermometers.

k) After dissolving the PMMA and annealing the whole devices at 400°C for several hours to further rid of any organic residues.

l) The device is cut out from the chip and ready for thermal measurements and sample characterization now.

On the one-inch chip, 25 small disks of 3mm in diameter was made particularly for TEM examination, as shown in Figure 4-2. There are three micro-thermometer devices on each disk, which amounts 75 micro devices on a chip.

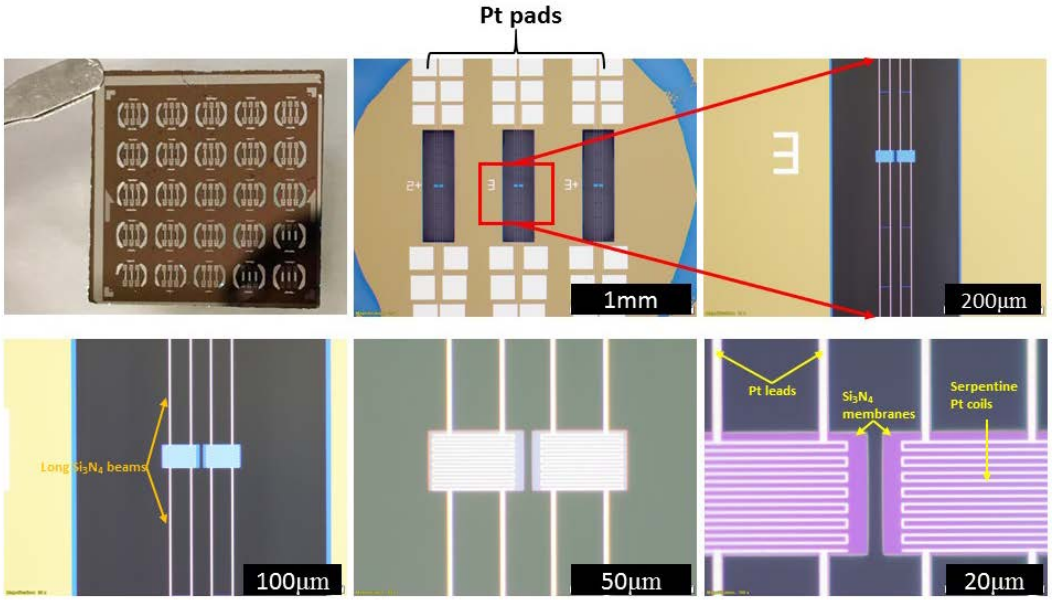

FIG. 4-2 Optical images of the micro thermal measurement devices. The first picture is the batched-fabricated chip, the following five pictures show the devices in ever higher magnifications and the components of the device are denoted in the pictures.

4.3.2 SAMPLE PREPARATION

The horizontally aligned single-walled carbon nanotube (HASWNT) will be transferred across the two-suspended sensing and heating membranes with PMMA thin film, shown in Figure 4-1(j). The sample preparation is demonstrated in Figure 4-3.

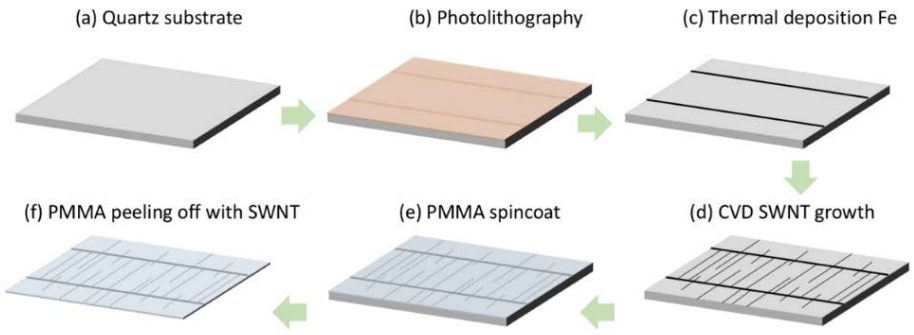

FIG. 4-3 Schematic diagram of sample preparation: HASWNT is grown between paralleled catalyst lines, and peeled off with PMMA to transfer onto micro thermal measurement chips.

a) The r-cut crystal quartz wafer is annealed in the air at 900°C for 12 hours.

b) The quartz wafer is undergone a photolithography to make the parallel catalyst patterns which is perpendicular to the preferable growth direction of SWNT. In this photolithography, photoresist JSR is spin-coated at 3000rpm for 30s ending with thickness around 2μm, exposed to ultra violet light for 3s and then developed in THAM for 60s to show the trenches for catalysts.

c) Later 0.2nm Fe is deposited in the trenches through thermal evaporation, and the photoresist will be dissolved in acetone with sonication. Afterwards, the wafer is cut into around one-inch size and annealed in the air at 500°C for five minutes.

d) Then a typical ACCVD process[32, 113] is conducted to grow HASWNT. The quartz substrate will go through a 40 minutes heating to 800°C under 300sccm Ar plus 3%H_2 gases to reduce iron oxide. After reduction, 450sccm ethanol will be introduced to provide carbon sources to grow HASWNT on the quartz substrate for 10 minutes to

obtain the proper density suitable for the suspended thermal measurements. After growth, the SEM images of HASWNT on quartz is show in Figure 4-4, and it is growth controlled to be low density[112] to avoid too much bundles formed after transfer.

e) PMMA (4% in anisole) is spin-coated on the after-growth quartz substrate at 3000rmp for 60s then baked at 180°C for 20 minutes.

f) As followed, the PMMA with HASWNT is peeled off in 5mol/L NaOH solution and transferred onto the micro thermometer device.

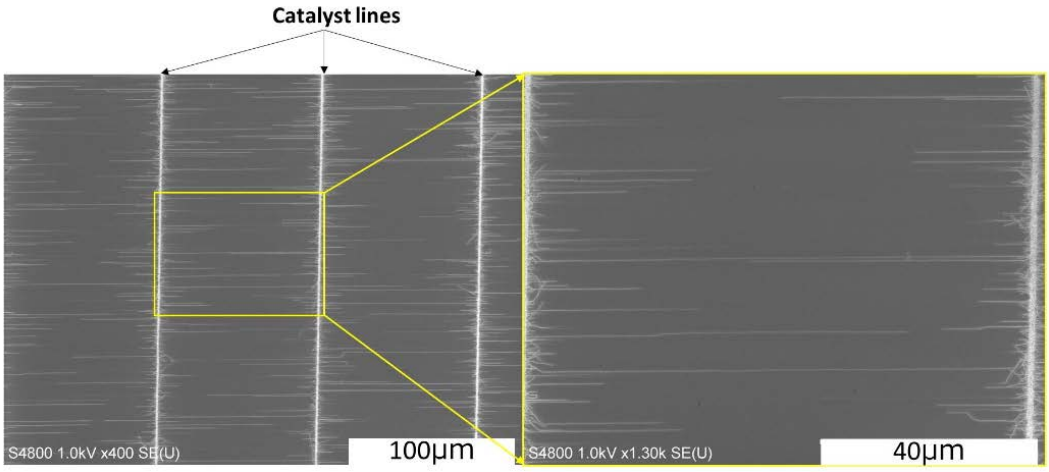

FIG. 4-4 HASWNT after growth on quartz substrate, the density is growth-controlled to be low.

4.3.3 SWNT CHARACTERIZATIONS

The successfully suspended SWNTs are shown in Figure 4-5 and Figure 4-6. SWNT bundles are unavoidably formed during transfer and annealing as the red arrow indicating in Figure 4-5, and they are much brighter than the single SWNTs in the SEM images. The gap sizes

in the upper and below panels in Figure 4-5 are 2μm and 4.5μm respectively, and there are three single SWNTs and a bundle in the upper panel, while there remains four single SWNTs and a bundle over the larger gap, which means the gap sizes has limited damages on the transferred SWNTs in this range. The SWNT or bundles can selectively be removed with a strong laser spot, since there is enough space between SWNTs. In Figure 4-6, five single SWNTs are over the 5μm trench, and by now all the preparation procedures are complete, thus they are ready for the thermal measurements. Meanwhile, the micro device with the same gap size but without suspended SWNTs will also be conducted with the experiment as the comparison to measure the background noises since they have gone through all of the same fabrication processes.

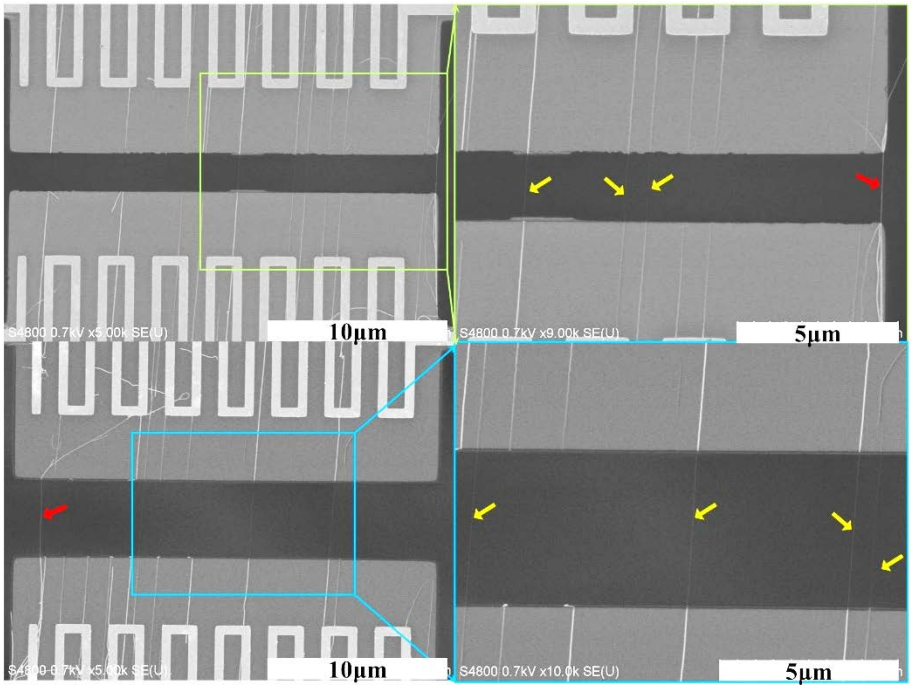

FIG. 4-5 Suspended SWNTs across the heating and sensing membranes. The red arrow is indicating SWNT bundles while the yellow arrow is pointing at single SWNTs. There are three single SWNTs and a bundle in the upper panel, the gap between membranes is 2μm; while in the below panel, over the 4.5μm gap there remains four single SWNTs and a bundle.

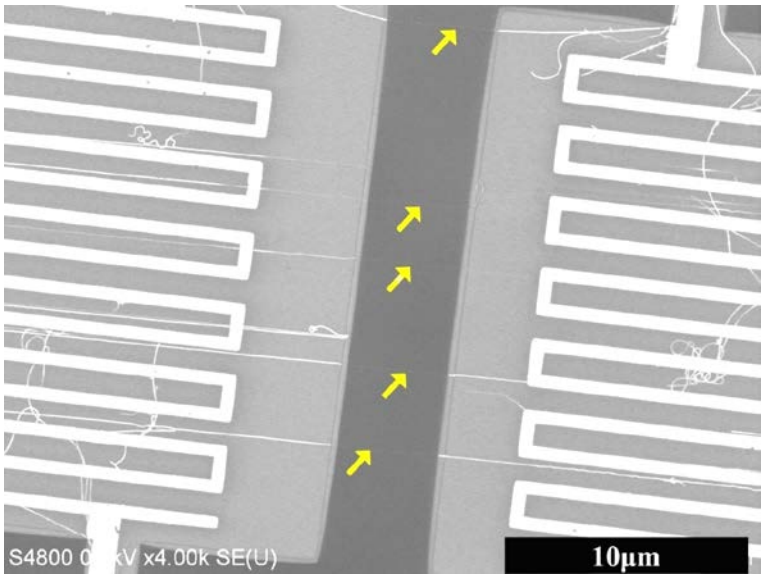

FIG. 4-6 Five single SWNTs are successfully transferred over the 5μm trench.

The ready-for-thermal-measurement samples were also examined in Transmission Electron Microscopy (TEM) which is a high-resolution method to explore the atomic structures of materials. In Figure 4-7 and Figure 4-8, the TEM images show that after several hours annealing at 400°C with a protection gas flow (300 sccm Ar+H_2) at 40kPa, the PMMA have completely decomposed and the samples are clean and clear in these images. Besides, through comparing the SEM and TEM images, a safe conclusion can be drawn that the carbon nanotube grown in this study are indeed single walled and no bundles are formed during growth. Therefore, the number of SWNTs in a bundle can be deduced by counting the extended SWNT on the Si_3N_4 membranes. On the upper membrane in the SEM image of Figure 4-7, three SWNTs formed a bundle and then separated into a single SWNT and a two-SWNT bundle; another single SWNT from the right side joined the two-SWNT bundle to form a three-SWNT bundle again. This

structure is also demonstrated in the middle TEM image of Figure 4-7 and the three-SWNT bundle is confirmed in the high magnification TEM image of the right in Figure 4-7.

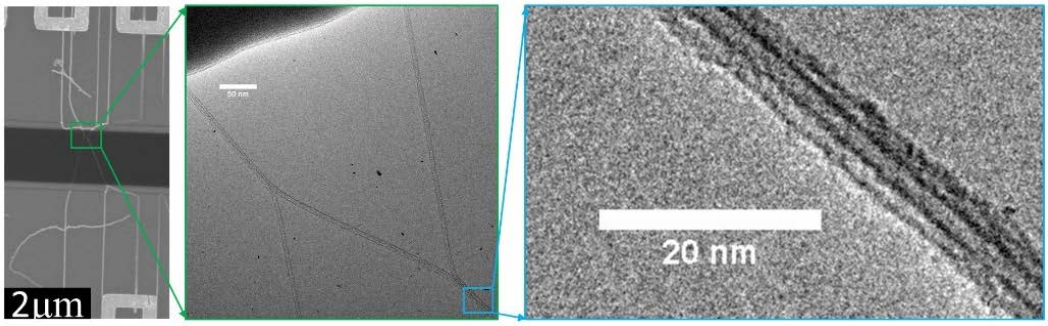

FIG. 4-7 Left: SEM image; Middle: TEM image, scale bar 50nm; Right: TEM image.

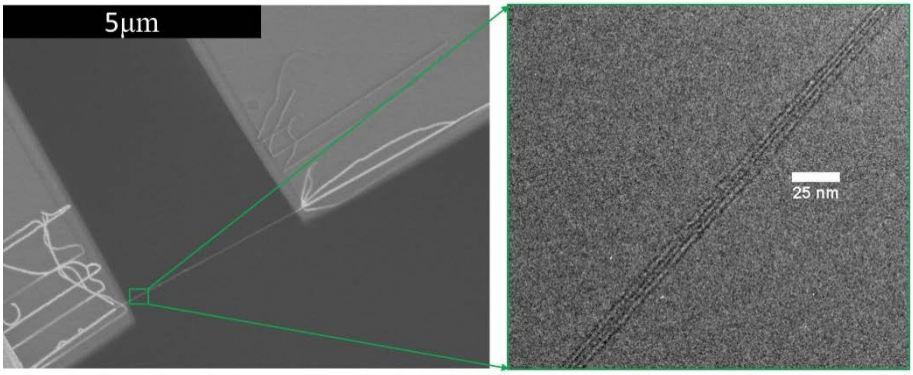

FIG. 4-8 SEM (Left) and TEM (Right) images of the ready-for-thermal-measurement sample.

4.3.4 MEASUREMENT SETUP

The micro-fabricated device is fixed in a high-vacuum cryostat (Janis, VPF-100), as demonstrated in Figure 4-9, through a cartridge heater and infilled liquid nitrogen, the temperature on the sample can be precisely controlled within a fluctuation of 20mK. The sample stage is further protected with a radiation shield, and the whole chamber will be pumped

overnight with a turbo molecular pump (TMP) and rotary pump.

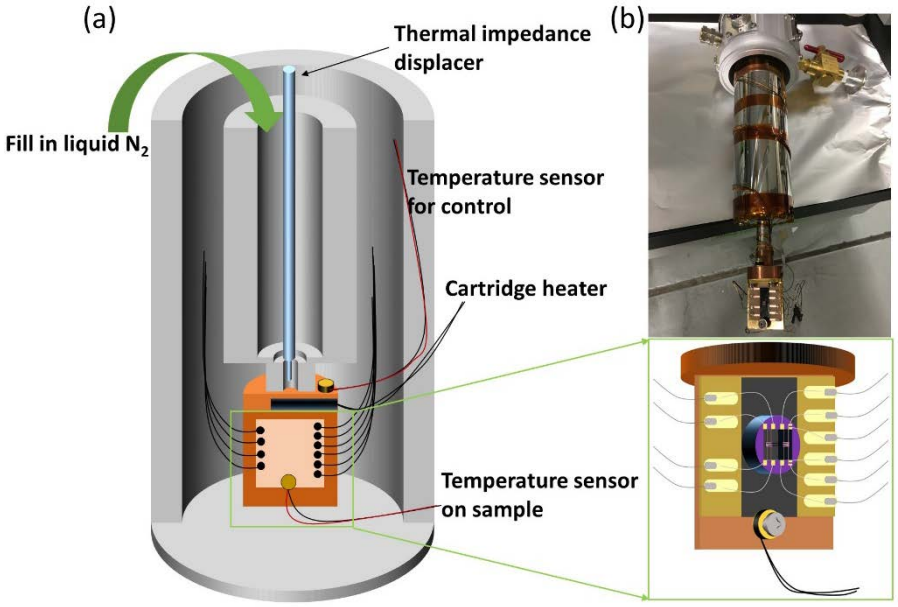

FIG. 4-9 (a) The schematic of the cryostat and (b) a photo of the practical device (Janis, VPF-100).

The measurement setup for the thermal properties investigation of SWNTs is illustrated in Figure 4-10. Two lock-in amplifiers are separately connected with the two micro-thermometers, denoted as heating membrane and sensing membrane respectively, to measure the resistance of the serpentine Pt coil on the membranes with a very high sensitivity. A typical four-point measurement is also conducted on the whole heating lines (serpentine Pt coil plus two Pt leads of the heating membrane) by Semiconductor Parameter Analyzer (Agilent, 4156C) to determine the resistance of the whole heating lines that also provides a DC current later to the suspended heating parts to generate enough Joule heating and form a steady-state heat flow in the suspended SWNTs at particular temperature. The feedback of the measurements is acquired and recorded by the computer for further analysis.

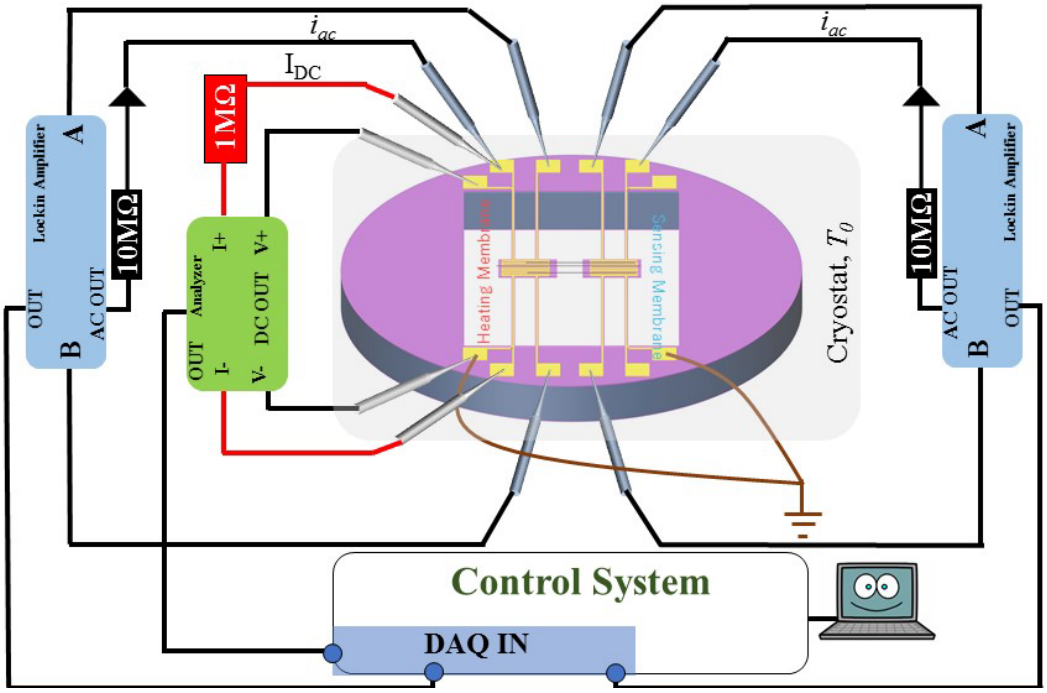

FIG. 4-10 Schematic illustration of the measurement setup for thermal transport properties of individual SWNTs.

4.3.5 THERMAL CONDUCTANCE MEASUREMENT

When a DC current is supplied to the serpentine Pt coil on the heating membrane through two Pt leads, they would generate Joule heats of Q_h (generated by the Pt coil) and $2Q_L$ (generated by two Pt leads) respectively, and increase the temperature of the heating membrane to T_h, which proved to be uniform on the whole membrane through simulation calculations[114, 115]. Afterwards, part of the heat Q_1 would dissipate to the environment through the four Si_3N_4 beams anchored to the heating membrane, and the other part of the heat Q_2 would be transported to the sensing membrane and cause its temperature rise to T_s by the SWNTs across the two

membranes, which finally would also spread to the environment at temperature of T_0 through the four Si_3N_4 beams connected with the sensing membrane. The heat flow and the thermal resistance circuit are schematically detailed in Figure 4-11. Of the nanoscale SWNT, the contact resistance cannot be ignored[114, 116, 117], which leads to the temperature of SWNT on the heating membrane is lower than T_h and higher than T_s on the sensing membrane. The sum of the contact conductance G_{c1} and G_{c2} on the membranes and the intrinsic thermal conductance of SWNT G_{swnt} is marked as G_s and can be directly measured in this experiment.

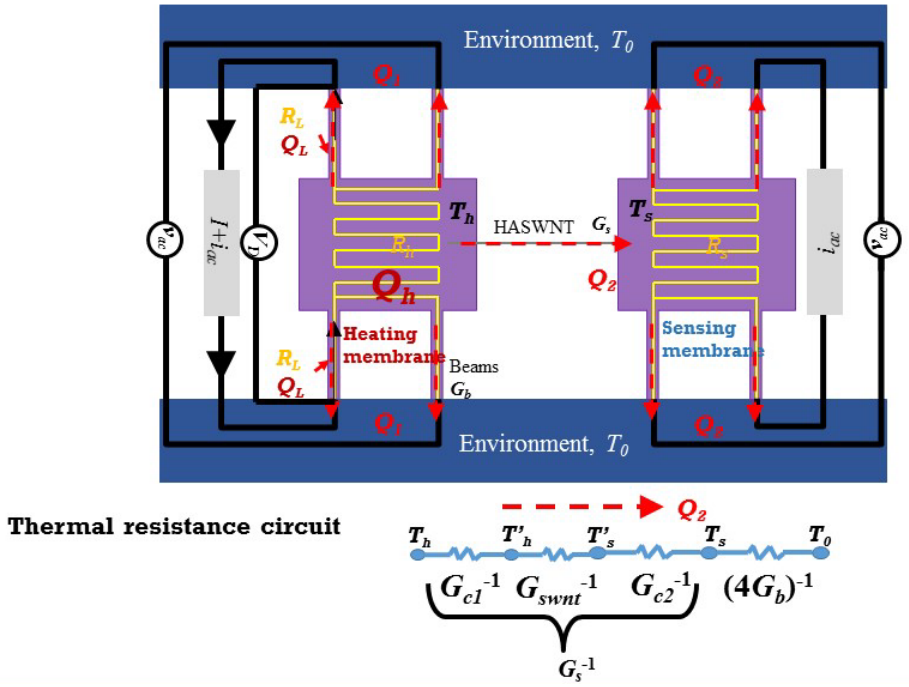

FIG. 4-11 Schematic diagram of the heat flow across the measurement setup and thermal conductance circuit in the experiment.

The temperature increases on the membranes can be determined by the resistance changes of the Pt coils through its TCR, and the resistance changes of the Pt coils can be detected

by a sensitive AC measurement provided by the Lock-in amplifiers[118].

$$TCR \equiv (dR/dT)/R \quad \text{Eq. (4-1)}$$

$$\Delta R_s(I) \equiv R_s(I) - R_s(I=0); \qquad \Delta T_s(I) = \frac{\Delta R_s(I)}{\frac{dR_s(I=0)}{dT}} \quad \text{Eq. (4-2)}$$

here, the subscript *s* is referring to the sensing membrane, while the *h* would be denoting heating membrane.

Moreover, the whole generated Joule heats Q_h+2Q_L can be determined by the following equation.

$$Q_h+2Q_L = I^2(R_h + 2R_L) \quad \text{Eq. (4-3)}$$

and R_h+2R_L is measured by the semiconductor parameter analyzer with the traditional four-point method before DC current heating at a particular temperature T_0. The temperature distribution in the six non-heating beams is linear, whereas it is parabolic in the two heating beams [115]. Therefore, according to the analyzed heat flow above illustrated in Figure 4-11, the heat conducted to the environment by the two heating beams of the heating membrane $Q_{hb,2}$, the heat conducted to the environment by the two non-heating beams on the heating membrane $Q_{h,2}$ and the heat ultimately also conducted to the environment by the four beams of the sensing membrane $Q_{s,4}$ are respectively expressed as

$$Q_{hb,2} = 2(G_b(T_h - T_0) + Q_L/2) \quad \text{Eq. (4-4)}$$

$$Q_{h,2} = 2G_b(T_h - T_0) \quad \text{Eq. (4-5)}$$

$$Q_{s,4} = 4G_b(T_s - T_0) \quad \text{Eq. (4-6)}$$

where G_b is the thermal conductance of the Si_3N_4 beam. Furthermore, the energy conservation

law predicts

$$Q_{hb,2} + Q_{h,2} + Q_{s,4} = Q_h + 2Q_L \qquad \text{Eq. (4-7)}$$

besides,

$$Q_1 = Q_h + 2Q_L - Q_2; \quad Q_2 = 4G_b(T_s - T_0) = G_s(T_h - T_s) \qquad \text{Eq. (4-8)}$$

as a result, what we are concerning most, the thermal conductance G_s can be determined through the following equations

$$G_b = \frac{Q_h + Q_L}{4(\Delta T_h + \Delta T_s)} \quad G_s = 4G_b \frac{\Delta T_s}{(\Delta T_h - \Delta T_s)} \qquad \text{Eq. (4-9)}$$

here, $\Delta T_h = T_h - T_0$; $\Delta T_s = T_s - T_0$.

As the most important intermediate term in investigation of the thermal conductance of sample, G_b is a self-inspection candidate for the reliability of the measurement system.

4.3.6 UNCERTAINTY ANALYSIS

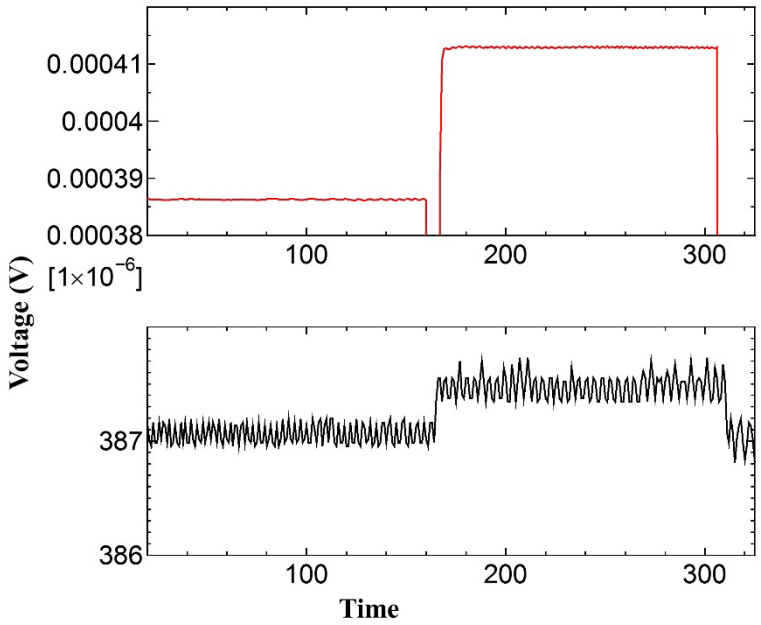

FIG. 4-12 Lock-in amplifier voltage response to DC current heating. The below panel is the voltage feedback of the Pt coil on the sensing membrane (input signal 100nA) while the upper panel is the voltage response on the heating membrane when the DC current changes from 0A to 8μA at the base temperature T_0 of 81.33K.

When the base temperature in the cryostat has been steady, the lock-in amplifier would record the voltage drop of the Pt coil on the membranes for a minute (the input signal of lock-in amplifier are 100nA AC current at 747.7Hz and 199.03Hz for heating membrane and sensing membrane respectively[119]), and then another minute with the constant DC current added in, as shown in Figure 4-12. The resistance is determined by averaging data in this one minute, which includes 100 data sets. The random uncertainty of resistance S_R is calculated by taking the standard deviation of the 100 data, which is less than 0.05% of the average values. The random resistance uncertainty before and during DC current heating S_{Rb} and S_{Rd} are transferred to the random uncertainty of the temperature change through

$$S_{\Delta T} = \frac{\sqrt{S_{Rb}^2 + S_{Rd}^2}}{\frac{dR(I=0)}{dT}} \qquad \text{Eq. (4-10)}$$

According to Eq. (4-9), the random uncertainty of the measured thermal conductance can be calculated by

$$S_{G_{s,m}} = (Q_h + Q_L)\sqrt{\left(\frac{2\Delta T_h \Delta T_s S_{\Delta T_h}}{\left(\Delta T_h^2 - \Delta T_s^2\right)^2}\right)^2 + \left(\frac{S_{\Delta T_s}}{\Delta T_h^2 - \Delta T_s^2} + \frac{2\Delta T_s^2 S_{\Delta T_s}}{\left(\Delta T_h^2 - \Delta T_s^2\right)^2}\right)^2} \qquad \text{Eq. (4-11)}$$

After background deduction, the thermal conductance of the sample is $G_s = G_{s,m} - G_{bg}$, and its uncertainty can be determined by

$$S_{G_s} = \sqrt{{S_{G_{s,m}}}^2 + {S_{G_{bg}}}^2} \qquad \text{Eq. (4-12)}$$

4.3.7 TEMPERATURE COEFFICIENT OF RESISTANCE

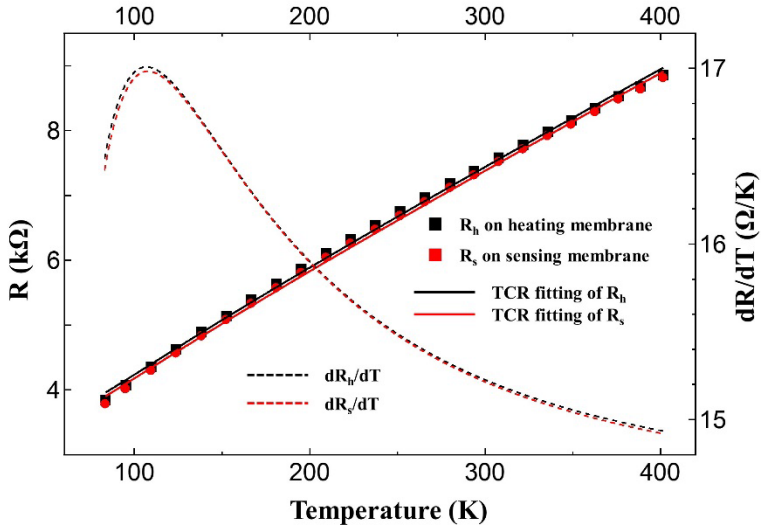

FIG 4-13 Measured resistance vs. temperature of the Pt coils on heating membrane (black filled squares) and sensing membrane (red filled dots), also the Bloch-Grüneisen relations are shown by solid lines.

The dashed curves are the extracted *dR/dT* from the Bloch- Grüneisen fitting formula.

The Bloch-Grüneisen formula is adopted to fit the experiment data R vs. T in order to determine the TCR (defined as dR/dT in this thesis) for the serpentine Pt coil thermometers:

$$R = R_0 + K_R \left(\frac{T}{\theta_D}\right)^5 \int_0^{\theta_D/T} \frac{x^5 dx}{(e^x - 1)(1 - e^{-x})} \qquad \text{Eq. (4-19)}$$

in which, R is the resistance, T is the temperature; R_0 is the residual resistance, θ_D is the Debye temperature, including K_R, these three are fitting parameters. The electron-phonon scattering that accounts for the temperature dependence of resistance is more accurately expressed in the Bloch-Grüneisen formula and it holds in the entire temperature range considered in the present work (80-410K), in comparison with the common linear or polynomial relations.

Figure 4-13 shows the experimental data as well as the fitted curve derived from the Bloch-Grüneisen formula, and they are in a very good agreement. With the fitted parameters, the TCR can be readily obtained by taking the temperature derivative of the resistance of the Bloch-Grüneisen formula as expressed in Eq. (4-20) and is plotted alongside the experimental data in Figure 4-13.

$$\frac{dR}{dT} = K_R \left(\frac{5T^4}{\theta_D^5}\right) \int_0^{\theta_D/T} \frac{x^5 dx}{(e^x - 1)(1 - e^{-x})} - K_R \left(\frac{T^3}{\theta_D^4}\right) \frac{(\theta_D/T)^5}{(e^{\theta_D/T} - 1)(1 - e^{-\theta_D/T})} \qquad \text{Eq. (4-20)}$$

Compared with the constant TCR (15.7Ω/K on the sensing membrane and 15.72Ω/K on the heating membrane) by linear fitting, the Bloch-Grüneisen fitting gives a changing TCR with temperature, from 16.42Ω/K and 16.49Ω/K at 83K and reaching a peak of 16.98Ω/K and 17.01Ω/K at 107K, then decrease to 14.92Ω/K and 14.93Ω/K at 402K on sensing membrane and

heating membrane respectively, avoiding about 7% deviation of the measured thermal conductance.

4.3.8 NOISE AND SENSITIVITY

The temperature rises on the heating membrane is far larger than that on the sensing membrane, and the true ΔT_s might be submerged with noises from the cryostat itself or the fluctuation in the measurement devices. Therefore, it is necessary to analyze the noise equivalent thermal conductance (NEG) caused by the noise temperature rise. According to Eq. (4-9),

$$G_{noise} = 4G_b \frac{\Delta T_{s,noise}}{(\Delta T_h - \Delta T_{s,noise})} \quad \text{Eq. (4-21)}$$

The random temperature fluctuation in the cryostat is approximately ΔT_0=20mK by the temperature controller, then the equivalent thermal conductance caused by it will be

$$G_{\Delta T_0} = 4G_b \frac{\Delta T_0}{(\Delta T_h - \Delta T_0)} \approx 4G_b \frac{\Delta T_0}{\Delta T_h} = 4G_b \left(\frac{dR_h}{dT}\right)\left(\frac{\Delta T_0}{\Delta R_h}\right) \quad \text{Eq. (4-22)}$$

which is on the order of 10^{-10}W/K at room temperature.

Another noise source is from the fluctuation of the resistance measurement. If the resistance fluctuation from the lock-in amplifier is $\Delta R_{s,electrical}$, then it will bring a noise temperature rise of $\Delta T_{s,electrical}$, resulting a noise equivalent conductance as the following equation.

$$G_{electrical} = 4G_b \frac{\Delta T_{s,electrical}}{(\Delta T_h - \Delta T_{s,electrical})} = 4G_b \frac{\Delta R_{s,electrical}}{\left(\frac{dR_S/dT}{dR_h/dT}\right)\Delta R_h - \Delta R_{s,electrical}} \quad \text{Eq. (4-23)}$$

Here, the fluctuation of resistance originates from the noises of the voltage and current supplied

by the lock-in amplifier,

$$\frac{\Delta R_{s,electrical}}{R_{s,0}} = \sqrt{\left(\frac{\Delta v_{ac}}{v_{ac}}\right)^2 + \left(\frac{\Delta i_{ac}}{i_{ac}}\right)^2} \quad \text{Eq. (4-24)}$$

where $R_{s,0}$ is the Pt resistance on the sensing membrane at the environment temperature T_0. The voltage fluctuation is dominated by Johnson noise and can be calculated by $\Delta v_{ac}=(4k_BT_sR_{s,0}\Delta f)^{1/2}\approx 7$nV, in which k_B is the Boltzmann's constant and Δf is the equivalent noise bandwidth around 0.26Hz in the experiment[119], thus $\Delta v_{ac}/v_{ac}$ is in the range of ~1×10^{-5}K^{-1}. The Poisson noise $\Delta i_{ac}=(2qi_{ac}\Delta f)^{1/2}\approx10^{-12}$ (q is the electron charge) has contributed to the AC current noise $(\Delta i_{ac}/i_{ac})^{*1}$ on the order of 1×10^{-5}K^{-1}. Besides, the AC current i_{ac} is converted from the internal constant AC voltage output from the lock-in amplifier v_{out} with a 10MΩ resistor, therefore partially

$$\left(\frac{\Delta i_{ac}}{i_{ac}}\right)^{*2} = \sqrt{\left(\frac{\Delta v_{out}}{v_{out}}\right)^2 + \left(\frac{\Delta R_{10\mathrm{M}\Omega}}{R_{10\mathrm{M}\Omega}}\right)^2} \quad \text{Eq. (4-25)}$$

here, the output voltage noise $\Delta v_{out}/v_{out}$ is about 5×10^{-5}K^{-1}, while the resistor fluctuation $\Delta R_{10\mathrm{M}\Omega}/R_{10\mathrm{M}\Omega}$ is 1×10^{-6}K^{-1}, so $\Delta i_{ac}/i_{ac}$ in this case is around 5×10^{-5}K^{-1}. Upon combination of the thermal and electrical noises, noise equivalent conductance by resistance fluctuation of Eq. (4-23) can be replaced by the following Eq. (4-26).

$$G_{electrical} = \frac{4G_b}{\left(\frac{dR_S/dT}{dR_h/dT}\right)\left(\frac{\Delta R_h}{\Delta R_{s,electrical}}\right)-1} = \frac{4G_b}{\left(\frac{dR_S/dT}{dR_h/dT}\right)\frac{\Delta R_h}{R_{s,0}\sqrt{\left(\frac{\sqrt{4k_BT_sR_{s,0}\Delta f}}{vac}\right)^2+\left(\frac{\sqrt{2qi_{ac}\Delta f}}{i_{ac}}\right)^2+\left(\frac{\Delta v_{out}}{v_{out}}\right)^2+\left(\frac{\Delta R_{10\mathrm{M}\Omega}}{R_{10\mathrm{M}\Omega}}\right)^2}}-1}$$

Eq. (4-26)

With the measured G_b which will discuss in the next section in Figure 4-15 and the TCR in Figure 4-13, $G_{electrical}$ can be estimated on the order of 10^{-10}W/K.

The sum of the above two effects is the total noise equivalent thermal conductance

$$G_{noise} = G_{\Delta T_0} + G_{electrical} \quad \text{Eq. (4-27)}$$

and is plotted in Figure 4-14.

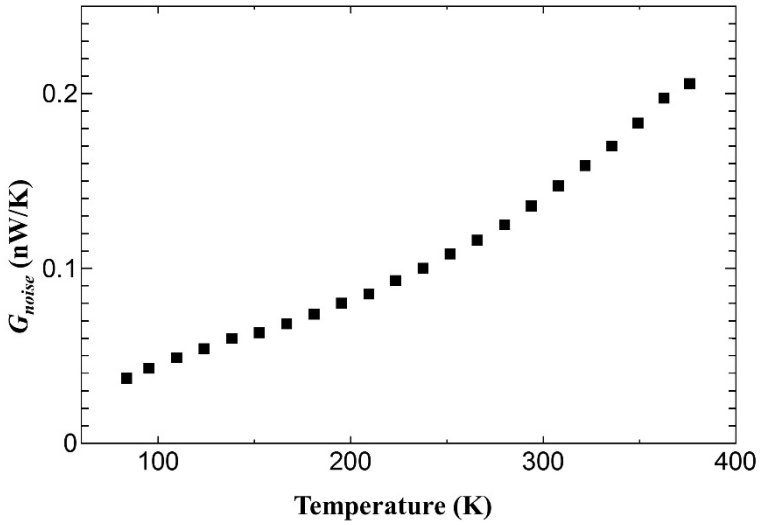

FIG 4-14 Sensitivity limit of the thermal conductance measurement with the temperature increase on the heating membrane about 10K and the base temperature fluctuation of 20mK.

The radiation and residual gas molecules are the main contributors for the background conductance to transfer part of the heat from the heating membrane to the sensing membrane. The radiation transfer between the two membranes can be approximated by

$$G_{bg,rad} = AF\sigma(T_h^2 + T_s^2)(T_h + T_s) \quad \text{Eq. (4-28)}$$

in which, *A*, *F*, σ are the cross-sectional area of the heating membrane, view factor between the heating and sensing membranes (~0.5) and Stefan-Boltzmann constant respectively. $G_{bg,rad}$ is in the range of 10^{-13}~10^{-11} from the lowest temperature to the highest temperature investigated in the present experiment, and below the sensitivity limit as discussed before. The radiation effects

from the heating beams on the resistance calculation are less than 10% through the finite element analysis[115].

The heat conduction from the heating membrane to the sensing membrane by the residual gas molecules can be calculated by

$$G_{bg,cond} = \frac{\kappa_{air} A}{L} \qquad \text{Eq. (4-29)}$$

here, κ_{air} is the pressure-dependent thermal conductivity of the air and is approximated on the order of 10^{-5} $Wm^{-1}K^{-1}$ at pressure of 10^{-2}Pa; L is the distance in-between the membranes. Therefore, $G_{bg,cond}$ can be obtained within the order of 10^{-11}W/K and also below the sensitivity limits of the experiment. However, the measured background conductance as plotted in Figure 4-16, ranges from ~3.5×10^{-11}W/K at 79K to ~3.5×10^{-10}W/K at 417K, higher than the calculated values in theory, too much to be ignored; indicating that the background measurements are necessary and compulsory to guarantee the precision of the thermal measurements.

4.4 EXPERIMENTAL RESULTS AND DISCUSSIONS

The thermal conductance measurements and sample identification were performed on the same single SWNTs or SWNT bundles across the two suspended micro-thermometer devices.

4.4.1 THERMAL CONDUCTANCE OF SUSPENDED BEAM

Since the whole heat generated in the micro thermometer device are ultimately dissipated to the environment through the eight identical Si_3N_4 beams, the thermal conductance of the suspended beam, the important self-inspection intermediate, predicts the functionality of the measurement system. Through Eq. (4-9), the thermal conductance of the suspended beam has been calculated at different temperatures and shown in Figure 4-15. The thermal conductance of the suspended beam includes contributions from the Si_3N_4 (thickness ~300nm) as well as the Pt lead thin film (thickness about 30nm~40nm). Therefore, for micro thermometer devices from different chips, the thermal conductance of the suspended beam will be a little divergent due to the KOH etching time and Pt sputtering time leading to different thickness of the Si_3N_4 and Pt thin film. In Figure 4-15, D1 is the thermal conductance of suspended beam from a particular chip, while D2B2 and D2B3 are the thermal conductance of suspended beams of two adjacent micro thermometer devices from another chip, which measured the SWNT samples B2 and B3 respectively. Micro thermometer of D2B2 and D2B3 have gone through the same fabrication processes, so the thermal conductance of their Si_3N_4 beams are within the error bar; whereas D1 from a different chip reasonably diverges from them at the higher temperature.

Taking into account the geometry of the suspended beam, as specified in Section 4.3.1, and the room temperature thermal conductivity values of SiN_x and Pt films from literature [12, 120], in which $\kappa_{SiNx}=5.5 Wm^{-1}K^{-1}$ and $\kappa_{Pt}=70 Wm^{-1}K^{-1}$, the thermal conductance of suspended beam can be obtained to be around 12.8nW/K, in good agreement with the values measured in Figure 4-15. Moreover, the measured temperature dependency of electrical resistance of Pt lead

on Si_3N_4 beam in Figure 4-16 shows the reverse trend with the thermal conductance of the beam, and the thermal conductivity of Pt thin film is inversely related with its electrical resistance, indicating that the discrepancy of the thermal conductance of different suspended beams mostly is due to the Pt thin film but Si_3N_4.

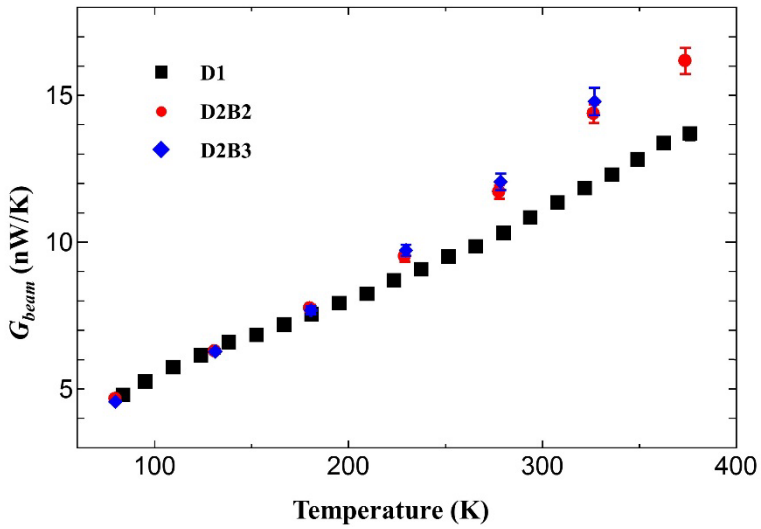

FIG. 4-15 The thermal conductance of the supporting Si_3N_4 beam increases with temperature. In the legend, D1 refers to the micro thermometer device on a particular 3-mm Disk 1; D2B1 and D2B2 are two adjacent micro thermometer devices on the same Disk 2, which measured the SWNT samples B2 and B3 respectively.

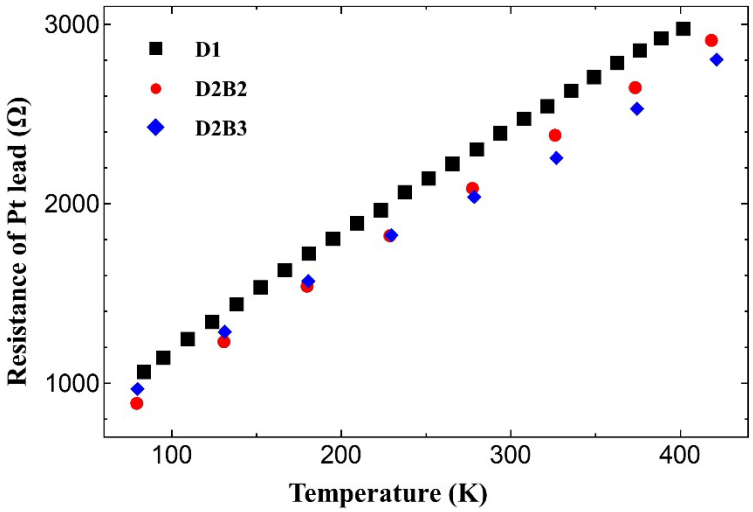

FIG. 4-16 The measured electrical resistance of Pt lead on the supporting Si_3N_4 beam.

4.4.2 THERMAL CONDUCTANCE OF SWNTS

As explained in Section 4.3.5, the measured thermal conductance can be obtained through Eq. (4-9), and plotted in Figure 4-17. Four different SWNT samples and the background without any SWNTs across the two suspended membranes are investigated in the temperature ranges from 78K to 410K. As elaborated before, the background thermal conductance contributed from the radiation and residual gas molecules conduction by theory are quite low, while the measured background thermal conductance indicated by the blank squares in Figure 4-17, in the range of 3.5×10^{-11} W/K to 3.5×10^{-10} W/K are much higher. This suggests more considerate modes for calculation of the radiation and residual gas molecules conduction.

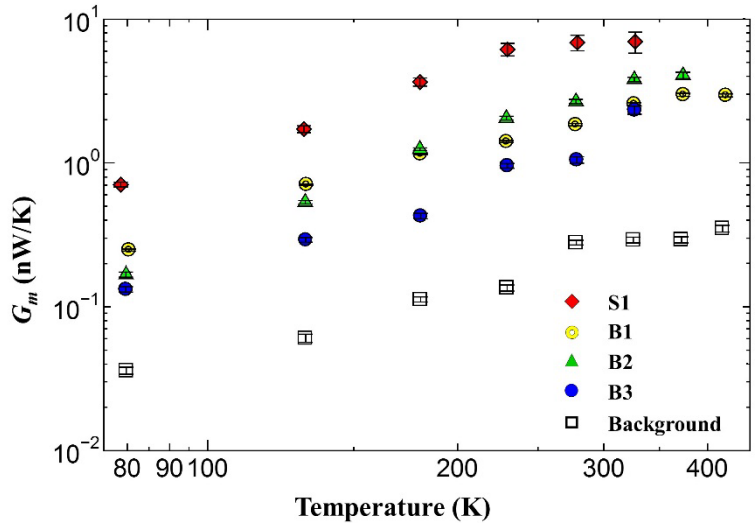

FIG. 4-17 The measured thermal conductance of four SWNT samples, denoted as S1, B1, B2 and B3, as well as the background thermal conductance.

After deduction the background thermal conductance from the measured thermal conductance of the samples, the thermal conductance of the SWNT samples is determined by $G_s = G_{s,m} - G_{bg}$, and its uncertainty can be calculated by Eq. (4-12), the results are demonstrated in Figure 4-18. The thermal conductance is increasing with the temperature first and saturate around 300K, in accordance with theoretical predictions[7, 121] and other experimental observations[13, 15].

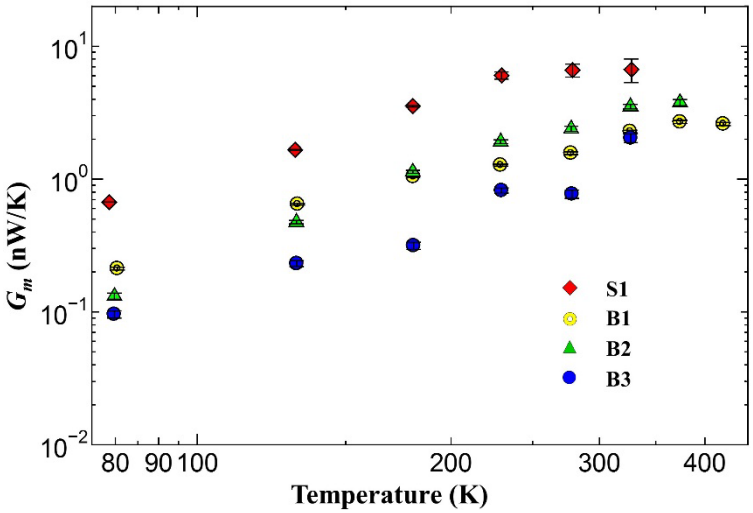

FIG. 4-18 The thermal conductance of four SWNT samples after background deduction.

4.4.3 SAMPLE IDENTIFICATION

As discussed in Section 4.3.3, the horizontally aligned carbon nanotubes grown on r-cut crystal quartz are single walled and no bundles formed during growth, and previous works[112, 122] in our lab through HASWNT characterization also suggested such conclusion. Therefore, the number of SWNTs in a bundle formed after transfer and annealing can be determined by counting the extended SWNTs on the membranes because the SWNTs are difficult to survive in TEM with 120kV accelerated electron beam.

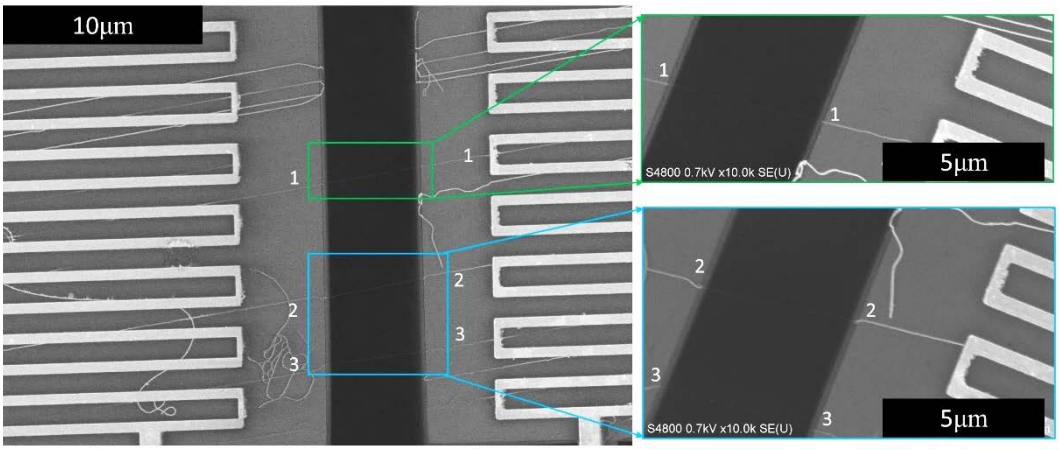

FIG. 4-19 SEM images of sample S1, composed of three single SWNTs, the gap between the two membranes is 5μm.

One of the four SWNT samples investigated in this study is denoted as S1, which includes three single SWNTs across the 5μm gap of the micro thermometer device, as the SEM images demonstate in Figure 4-19, in which number 1 to 3 are pointing at the extended ends of those SWNTs on the membranes. The other three SWNT samples are denoted as B1, B2 and B3 respectively, which are SWNT bundles composed of thirteen, four and eight SWNTs as shown and specified in Figure 4-20, Figure 4-21 and Figure 4-22 accordingly. It is worth to be noted also in those images that the transferred HASWNTs remain tens of micrometers on both membranes to keep the suspended part very straight over the gap.

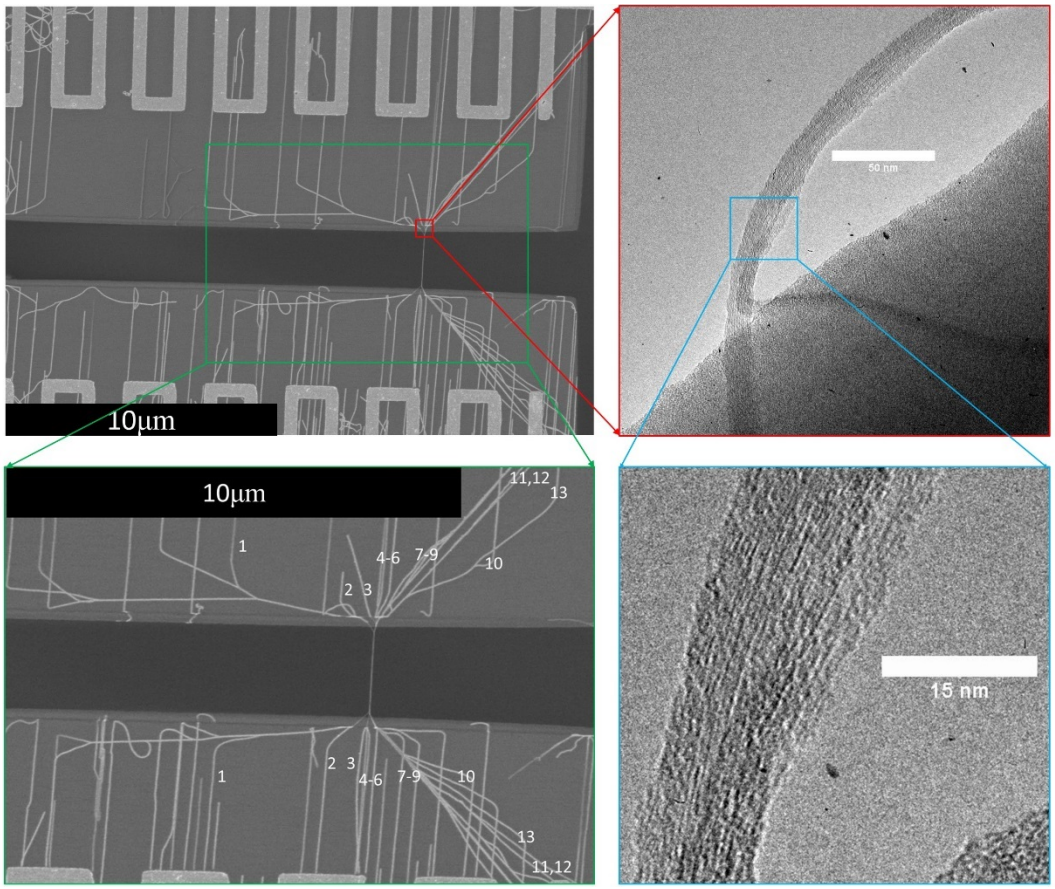

FIG. 4-20 SEM images of sample B1, an SWNT bundle of thirteen SWNTs, the gap between the two membranes is 2.5μm; the TEM images on the right side is taken after the SWNT bundle is broken.

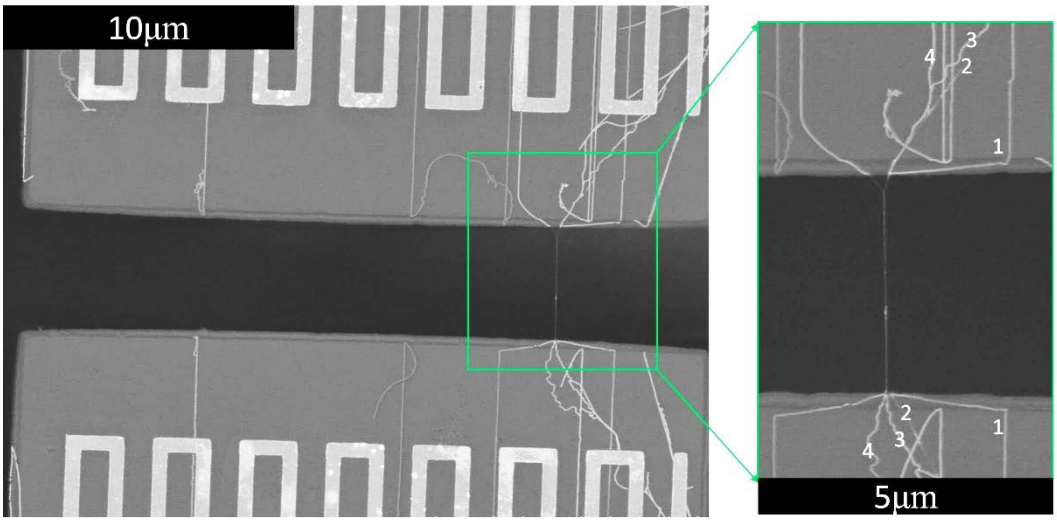

FIG. 4-21 SEM images of sample B2, an SWNT bundle of four SWNTs, the gap between the two membranes is 4.5μm.

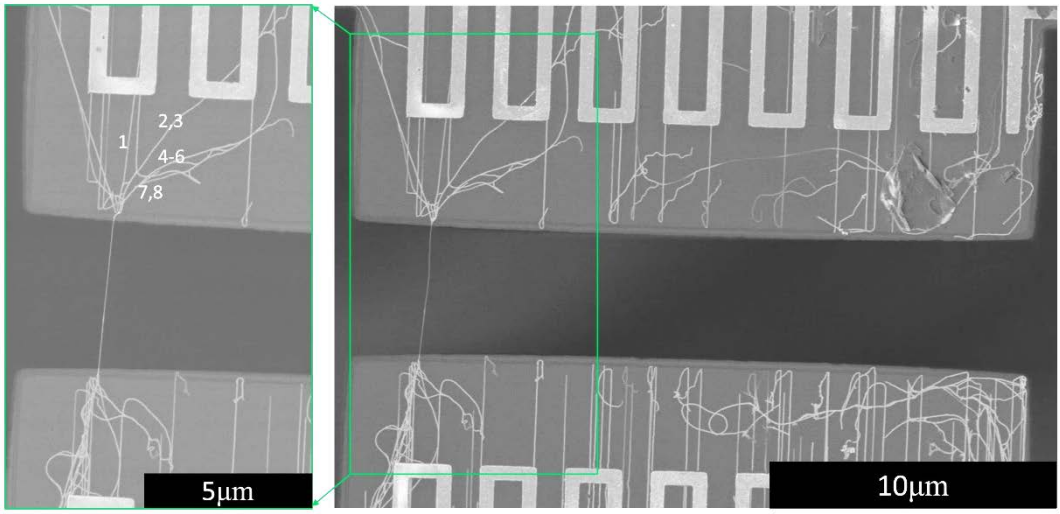

FIG. 4-22 SEM images of sample B3, an SWNT bundle of eight SWNTs, the gap between the two membranes is 5μm.

4.4.4 THERMAL BOUNDARY RESISTANCE

To account for the thermal boundary resistance (TBR), the interface thermal coupling per unit length (g, $Wm^{-1}K^{-1}$) developed for CNT-SiO_2 interactions by molecular dynamics simulation in consideration of the lattice contribution to thermal transport[123] is adopted, which is expressed as

$$g \approx 0.05D\chi\left(\frac{T}{200}\right)^{1/3} \quad \text{Eq. (4-30)}$$

here, D is the diameter of CNT in nanometer and T is temperature in Kelvins; χ is the CNT-substrate interaction strength.

Assuming the average contact length per SWNT on the membrane surface is 40μm as

Figure 4-19 have shown for S1, and the average diameter of SWNT is 2nm[112] and χ=1, the thermal boundary resistance of the sample S1 is calculated with Eq. (4-30) and plotted in the temperature range from 75K to 420K as demonstrated in Figure 4-23, which is in consistent with other analyses and measurements[42, 124, 125]. The thermal boundary resistance is hugely consumed by the long parts of SWNTs on the membranes, better than the limited increase of contact area by Pt-C deposition[126].

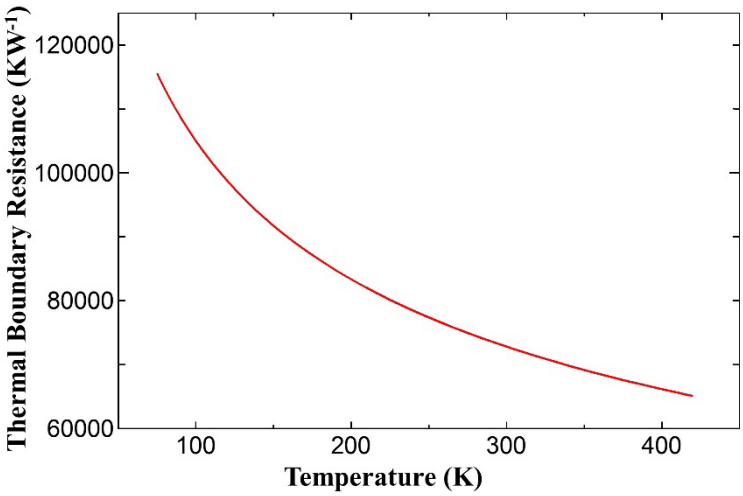

FIG. 4-23 Calculated thermal boundary resistance for sample S1 versus temperature.

In comparison with the direct CNT growth[19, 45, 127] on the micro thermometer or CNT solution dropping[12], the annealing after PMMA transfer is hugely increased the contacts between SWNT and the substrate. Therefore, the SWNTs after PMMA decomposition is still well aligned and the suspended parts are perfectly straight, as shown in the previous SEM images. The extended SWNTs on the membranes of bundles is dispersive hence fold increases the contact areas and decreases the thermal boundary resistance. With the uniform temperature on the

membranes[115], the thermal boundary resistance become negligible consequently in this study. As shown in Figure 4-24, the measured total thermal resistance of S1 is four magnitude larger than the calculated thermal boundary resistance.

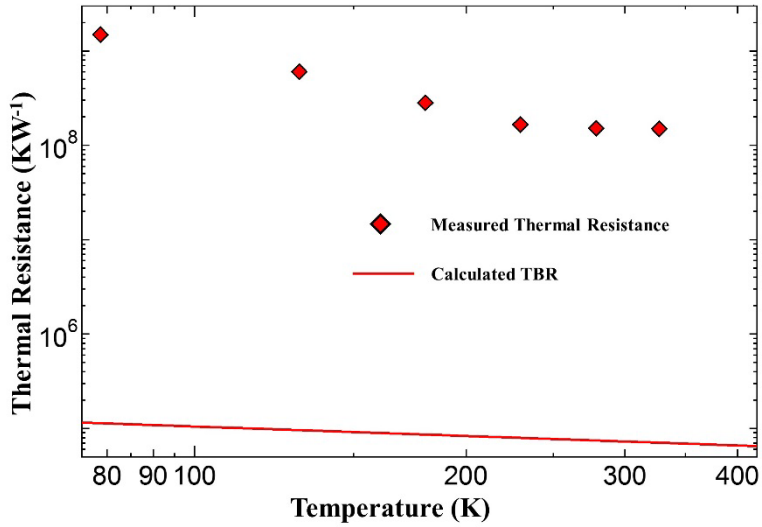

FIG. 4-24 The measured total thermal resistance of S1 and the calculated thermal boundary resistance.

4.4.5 EFFECTIVE THERMAL CONDUCTIVITY

The above analysis legitimates the acquisition of effective thermal conductivity of the samples in this study by $\kappa=G_sL/A$, where L and A are the suspended SWNTs length and cross-sectional area of the samples, respectively. Assuming the diameter of SWNT to be 2nm (based on the diameter distribution on quartz growth from previous study[112] and TEM characterization in this study), the cross-sectional area of a SWNT can be calculated with $\pi\delta D$, in which δ is the thickness of monolayer graphene 0.34nm[128]. Figure 4-25 shows the effective

thermal conductivity obtained for single SWNT (S1) and SWNT bundles (B1, B3 and B3).

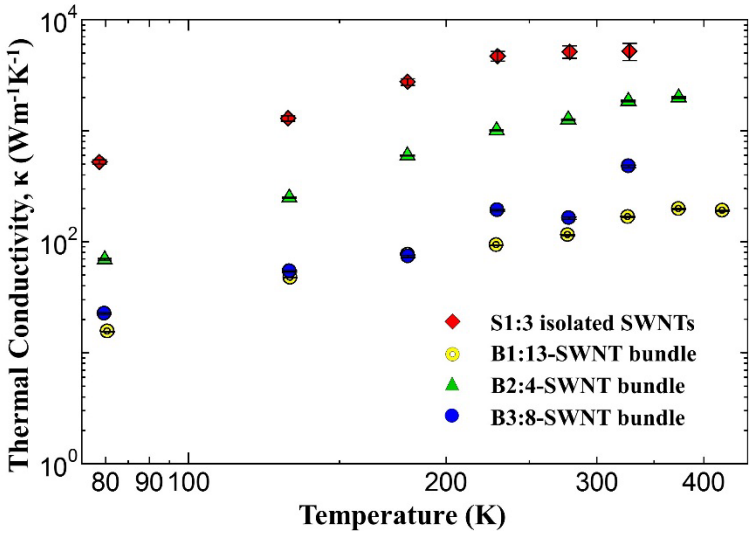

FIG. 4-25 The effective thermal conductivity of four samples versus temperature.

The isolated SWNT possesses the highest thermal conductivity, around 5000$Wm^{-1}K^{-1}$ at room temperature (RT), whereas the thermal conductivity is much lower in SWNT bundles, and decreases with the bundles sizes (B2: four-SWNT bundle >B3: eight-SWNT bundle> B1: thirteen-SWNT bundle). This degeneration of thermal conductivity resulting from bundles can attribute to the inter-tube interactions that profoundly increases three-phonon Umklapp scatterings involving phonons from neighboring SWNTs[129], and it is consistent with other experimental observations[12, 14, 127, 130, 131]. Moreover, this conclusion verifies the measured relatively higher thermal conductivity of the SWNT thin films in the last Chapter, which are composed of smaller SWNT bundles and even fraction of isolated SWNT. Figure 4-26 plots the effective thermal conductivity logarithmically decreases with the increased number of SWNT in a bundle, and this is the first-time quantitative study of the thermal conductivity

dependency on SWNT bundle size.

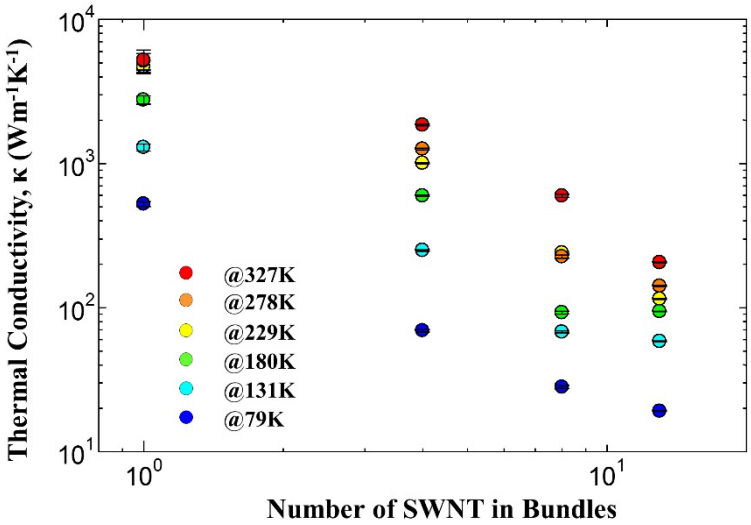

FIG. 4-26 The effective thermal conductivity versus number of SWNT in a bundle.

Kinetic theory[132] (phonon gas) predicts the thermal conductivity in insulators or semiconductor materials as follows:

$$\kappa = \frac{1}{3} C v^2 \tau; \qquad \text{Eq. (4-31)}$$

where C is the lattice volumetric specific heat, v is the average speed of corresponding phonons, and τ is the approximated relaxation time. Besides, τ is the reciprocal of collision rate (γ) between phonons. For an isolated SWNT, its average collision rate is $\gamma_{isolated}$, and the addition of N SWNTs will increase the collision rate by $\gamma_{bundle}(N)$ which is proportional to the increased number of interactions per nanotube in the bundle.

$$\tau = \frac{1}{\gamma}; \quad \gamma = \gamma_{isolated} + \gamma_{bundle}(N) \qquad \text{Eq. (4-32)}$$

$$\gamma_{bundle}(N) \propto Number\ of\ interactions\ per\ tube \qquad \text{Eq. (4-33)}$$

Therefore, the thermal conductivity in SWNTs can be expressed as Eq. (4-34).

$$\kappa = \frac{1}{3} C v^2 \frac{1}{\gamma_{isolated} + \gamma_{bundle}(N)} \quad \text{Eq. (4-34)}$$

The thermal conductivity is inversely proportional to the phonons collision rate; with the increase of bundle size, there are increased chances of collision with the neighboring carbon nanotubes. The experimental data is fitted with Eq. (4-34) and shown in Figure 4-27, and they agree well, indicating that the interactions with neighboring SWNT is inelastic scattering and strongly quenches phonon modes in bundles that leads to the very low thermal conductivity of bundled SWNTs.

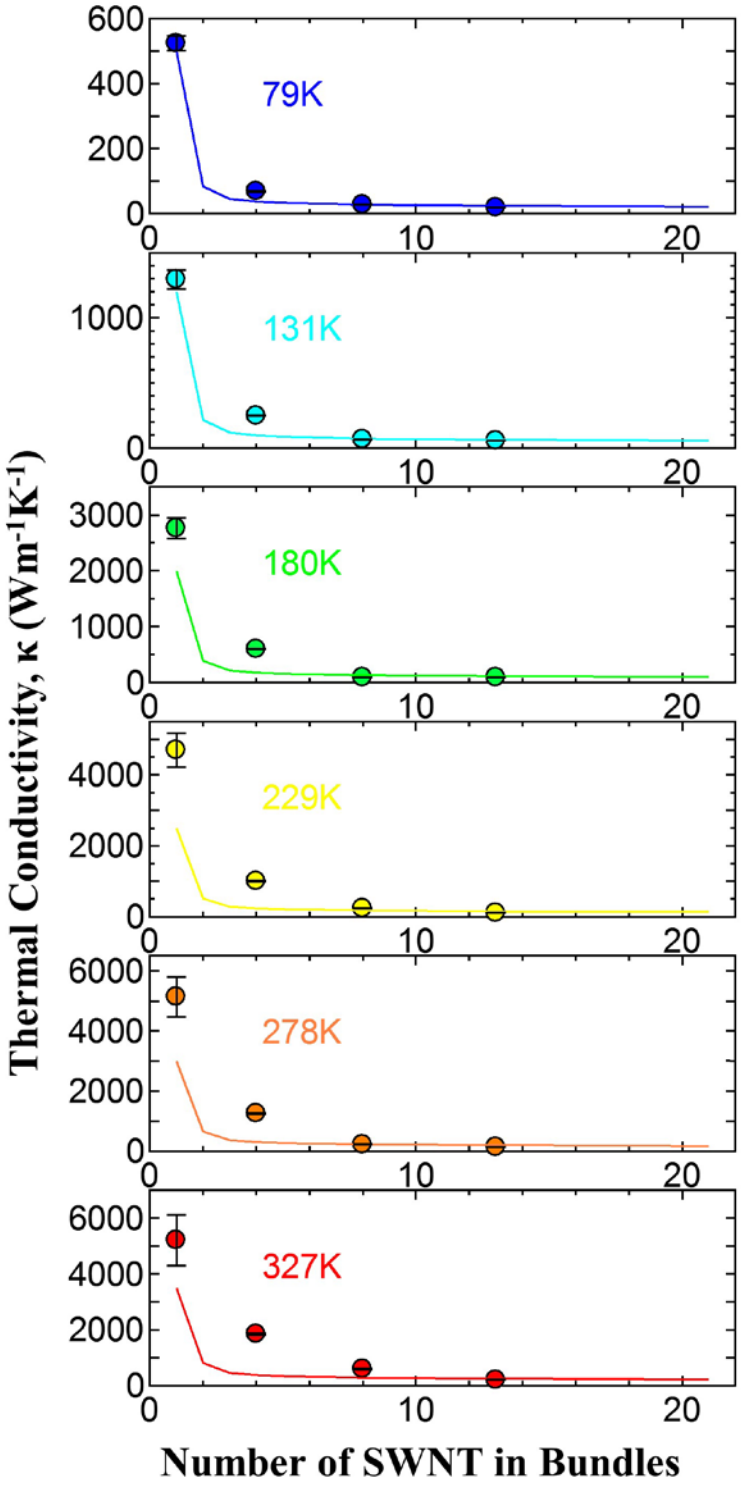

FIG. 4-27 Fitting the experimental data with collision rate through kinetic theory.

4.5 CONCLUSIONS

The micro thermometer device compatible with TEM has been fabricated and the measurement setup has been established to investigate the axial thermal conductance of individual SWNTs. The SEM and TEM images show that the transferred horizontally aligned carbon nanotubes across the micro-thermometers are very clean and straight; and the number of SWNT in a bundle can be determined by counting the dispersedly extended SWNTs on the supporting membranes.

Four different samples are studied in this study, which are S1, composed of three single SWNTs; B1, a thirteen-SWNT bundle; B2, a four-SWNT bundle and B3, an eight-SWNT bundle. Due to the large overlap areas of SWNTs and supporting membranes, the thermal boundary resistance is hugely decreased and can be ignored in calculation of effective thermal conductivity of SWNTs.

The obtained thermal conductivity is the highest for the sample with three isolated SWNTs, reaching $5000 Wm^{-1}K^{-1}$ around RT. The bundles possess much degenerated thermal conductivity, and the larger the bundle, the lower its thermal conductivity. This is the first time that the thermal conductivity of SWNT have been quantitatively studied in relation to the bundle size. The logarithmical degeneration of thermal conductivity resulting from bundles can attribute to the increased collision rate with neighboring SWNTs that impedes the phonon transport of

isolated SWNTs, and it agrees well with the analysis by kinetic theory, indicating much stronger interactions between carbon nanotubes. Moreover, this conclusion verifies the measured relatively higher thermal conductivity of the SWNT thin films in the last Chapter, which are composed of less bundled SWNTs.

CHAPTER 5 SUMMARY

The thermal properties of CNTs are demanding to be clarified with the fast approaching application of CNT electronics. In nanoscale, the relationship of the thermal properties of SWNT and its nanoscale structure determines the fundamental architecture of CNT electronics; it also can help to understand the bulk properties in macro-scale SWNT films.

To address the problem of limited method to study the structure dependency of thermal transport properties of macro-scale SWNT thin films, a quick and contact-free method for the measurement of in-plane sheet thermal conductance of SWNT thin films with the steady-state infrared thermography have been proposed in this thesis. Four different SWNT thin films have been investigated with this new method and the results indicate the sheet thermal conductance are 15613.4 ± 2672.5nW/K, 9925.4 ± 1417.1nW/K, 5454.8 ± 594.9nW/K and 3405.7 ± 773.8nW/K at room temperature for the films with transparency of 60%, 70%, 80% and 90% (thickness related), respectively. In comparison with the Raman measurements of the same SWNT thin films, the strong non-equilibrium of different phonon polarizations and electrons are expected to contribute to the lower thermal conductivity by a factor of 1.9-2.5 in Raman measurements. The relatively higher thermal conductivity of the SWNT thin films in this study also suggests that the smaller bundles sizes in its composition might refrain the thermal transport properties from further degradation.

To study how the nanoscale thermal behavior of SWNT affects the macro-scale SWNT

networks or the bundle dependency, the micro-thermometer compatible with TEM has been successfully fabricated and the auxiliary thermal measurement setup has been established to explore the bundle size dependency of thermal conductivity in individual SWNTs. Four different samples are studied in this study, which are S1, composed of three single SWNTs; B1, a thirteen-SWNT bundle; B2, a four-SWNT bundle and B3, an eight-SWNT bundle. Due to the large overlap areas of SWNTs and supporting membranes, the thermal boundary resistance is hugely decreased and can be ignored in calculation of effective thermal conductivity of SWNTs. The obtained thermal conductivity is the highest for the sample with three isolated SWNTs. The bundles possess much degenerated thermal conductivity, and the thermal conductivity logarithmically decreases with the increased number of SWNT in a bundle, verifying the speculation in the IR measurements; the degeneration of thermal conductivity in larger SWNT bundles owes to the increased inelastic scattering with neighboring SWNTs. It is the first time the thermal conductivity of SWNT have been quantitatively studied regarding the bundle size.

In this thesis, two different systems have been established to study the macro-scale and nanoscale thermal transport properties of SWNTs. The correlation of thermal transport properties between the nanoscale and macro-scale in SWNTs are expected to be more specifically founded in the near future and contribute to the application of CNTs.

BIBLIOGRAPHY

1. Moore, A.L. and L. Shi, *Emerging challenges and materials for thermal management of electronics.* Materials Today, 2014. **17**(4): p. 163-174.

2. Berber, S., Y.-K. Kwon, and D. Tomanek, *Unusually high thermal conductivity of carbon nanotubes.* Physical Review Letters, 2000. **84**(20): p. 4613-4616.

3. Maruyama, S., *A molecular dynamics simulation of heat conduction in finite length SWNTs.* Physica B: Condensed Matter, 2002. **323**(1): p. 193-195.

4. Maruyama, S., et al., *Anisotropic Heat Transfer of Single-Walled Carbon Nanotubes.* Journal of Thermal Science and Technology, 2006. **1**(2): p. 138-148.

5. Shiomi, J. and S. Maruyama. *Diameter and length effect on diffusive-ballistic phonon transport in a carbon nanotube*. in *ASME-JSME Thermal Engineering Summer Heat Transfer Conference*. 2007.

6. Mingo, N. and D. Broido, *Length dependence of carbon nanotube thermal conductivity and the "problem of long waves"*. Nano Letters, 2005. **5**(7): p. 1221-1225.

7. Lukes, J.R. and H. Zhong, *Thermal Conductivity of Individual Single-Wall Carbon Nanotubes.* Journal of Heat Transfer, 2007. **129**(6): p. 705.

8. Choi, T.Y., et al., *Measurement of thermal conductivity of individual multiwalled carbon nanotubes by the 3-ω method.* Applied Physics Letters, 2005. **87**(1): p. 013108.

9. Fujii, M., et al., *Measuring the thermal conductivity of a single carbon nanotube.* Physical review letters, 2005. **95**(6): p. 065502.

10. Choi, T.-Y., et al., *Measurement of the thermal conductivity of individual carbon nanotubes by the four-point three-ω method.* Nano letters, 2006. **6**(8): p. 1589-1593.

11. Shaikh, S., et al., *Thermal conductivity of an aligned carbon nanotube array.* Carbon, 2007. **45**(13): p. 2608-2613.

12. Shi, L., et al., *Measuring thermal and thermoelectric properties of one-dimensional nanostructures using a microfabricated device.* Journal of heat transfer, 2003. **125**(5): p. 881-888.

13. Kim, P., et al., *Thermal transport measurements of individual multiwalled nanotubes.* Physical review letters, 2001. **87**(21): p. 215502.

14. Yu, C., et al., *Thermal conductance and thermopower of an individual single-wall carbon nanotube.* Nano Letters, 2005. **5**(9): p. 1842-1846.

15. Pop, E., et al., *Thermal conductance of an individual single-wall carbon nanotube above room temperature.* Nano Letters, 2006. **6**(1): p. 96-100.

16. Wang, Z.L., et al., *Length-dependent thermal conductivity of an individual single-wall carbon nanotube.* Applied Physics Letters, 2007. **91**(12): p. 123119.

17. Li, Q., et al., *Measuring the thermal conductivity of individual carbon nanotubes by the Raman shift method.* Nanotechnology, 2009. **20**(14): p. 145702.

18. Marconnet, A.M., M.A. Panzer, and K.E. Goodson, *Thermal conduction phenomena in carbon nanotubes and related nanostructured materials.* Reviews of Modern Physics, 2013. **85**(3): p. 1295-1326.

19. Pettes, M.T. and L. Shi, *Thermal and Structural Characterizations of Individual Single-, Double-, and Multi-Walled Carbon Nanotubes.* Advanced Functional Materials, 2009. **19**(24): p. 3918-3925.

20. Prasher, R.S., et al., *Turning carbon nanotubes from exceptional heat conductors into insulators.* Physical review letters, 2009. **102**(10): p. 105901.

21. Kim, D., et al., *Raman Characterization of Thermal Conduction in Transparent Carbon Nanotube Films.* Langmuir, 2011. **27**(23): p. 14532-14538.

22. Sahoo, S., et al., *Thermal Conductivity of Freestanding Single Wall Carbon Nanotube Sheet by Raman Spectroscopy.* ACS applied materials & interfaces, 2014. **6**(22).

23. Aliev, A.E., et al., *Thermal conductivity of multi-walled carbon nanotube sheets: radiation losses and quenching of phonon modes.* Nanotechnology, 2010. **21**(3): p. 035709.

24. Lian, F., et al., *Thermal Conductivity of Chirality-Sorted Carbon Nanotube Networks.* arXiv preprint arXiv:1601.07560, 2016.

25. Hone, J., et al., *Electrical and thermal transport properties of magnetically aligned single wall carbon nanotube films.* Applied Physics Letters, 2000. **77**(5): p. 666.

26. Lee, V., et al., *Divergent and ultrahigh thermal conductivity in millimeter-long nanotubes.* Phys. Rev. Lett., 2017. **118**: p. 135901.

27. Avery, A.D., et al., *Tailored semiconducting carbon nanotube networks with enhanced thermoelectric properties.* Nature Energy, 2016. **1**: p. 16033.

28. Kroto, H.W., et al., *C 60: buckminsterfullerene.* Nature, 1985. **318**(6042): p. 162-163.

29. Iijima, S., *Helical microtubules of graphitic carbon.* nature, 1991. **354**(6348): p. 56-58.

30. Iijima, S. and T. Ichihashi, *Single-shell carbon nanotubes of 1-nm diameter.* Nature, 1993. **363**(6430): p. 603-605.

31. Ren, Z., et al., *Synthesis of large arrays of well-aligned carbon nanotubes on glass.* Science, 1998. **282**(5391): p. 1105-1107.

32. Maruyama, S., et al., *Low-temperature synthesis of high-purity single-walled carbon nanotubes from alcohol.* Chemical Physics Letters, 2002. **360**(3): p. 229-234.

33. Saito, R., G. Dresselhaus, and M.S. Dresselhaus, *Physical properties of carbon nanotubes*. 1998: World scientific.

34. Dresselhaus, M.S., et al., *Raman spectroscopy of carbon nanotubes.* Physics Reports, 2005. **409**(2): p. 47-99.

35. Dresselhaus, M. and P. Eklund, *Phonons in carbon nanotubes.* Advances in Physics, 2000. **49**(6): p. 705-814.

36. Feng, Y., J. Zhu, and D.-W. Tang, *Molecular dynamics study on heat transport from single-walled carbon nanotubes to Si substrate.* Physics Letters A, 2015. **379**(4): p. 382-388.

37. Hone, J., et al., *Thermal properties of carbon nanotubes and nanotube-based materials.* Applied Physics A: Materials Science & Processing, 2002. **74**(3): p. 339-343.

38. Hone, J., M. Whitney, and A. Zettl, *Thermal conductivity of single-walled carbon nanotubes.* Synthetic metals, 1999. **103**(1-3): p. 2498-2499.

39. Shi, L., *Thermal and Thermoelectric Characterization of Individual Nanostructures and Thin Films*, in *Materials, Preparation, and Characterization in Thermoelectrics*. 2012, CRC Press. p. 1-26.

40. Weathers, A. and L. Shi, *Thermal transport measurement techniques for nanowires and nanotubes.* Annual Review of Heat Transfer, 2013. **16**(16).

41. Cahill, D.G., *Thermal conductivity measurement from 30 to 750 K: the 3ω method.* Review of scientific instruments, 1990. **61**(2): p. 802-808.

42. Pop, E., et al., *Electrical and thermal transport in metallic single-wall carbon nanotubes on insulating substrates.* Journal of Applied Physics, 2007. **101**(9): p. 093710-093710-10.

43. Wingert, M.C., et al., *Ultra-sensitive thermal conductance measurement of one-dimensional nanostructures enhanced by differential bridge.* Review of Scientific Instruments, 2012. **83**(2): p. 024901.

44. Hsu, I.K., et al., *Optical measurement of thermal transport in suspended carbon nanotubes.* Applied Physics Letters, 2008. **92**(6): p. 063119.

45. Hsu, I.-K., et al., *The effect of gas environment on electrical heating in suspended carbon nanotubes.* Journal of Applied Physics, 2010. **108**(8): p. 084307-084307-4.

46. Chiashi, S., et al., *Temperature dependence of Raman scattering from single-walled carbon nanotubes: Undefined radial breathing mode peaks at high temperatures.* Japanese Journal of Applied Physics, 2008. **47**(4R): p. 2010.

47. De Volder, M.F.L., et al., *Carbon Nanotubes: Present and Future Commercial Applications.* Science, 2013. **339**(6119): p. 535-539.

48. Baughman, R.H., A.A. Zakhidov, and W.A. de Heer, *Carbon nanotubes--the route toward applications.* Science, 2002. **297**(5582): p. 787-92.

49. Liu, C., et al., *Hydrogen storage in single-walled carbon nanotubes at room temperature.* Science, 1999. **286**(5442): p. 1127-1129.

50. Fan, S., et al., *Self-oriented regular arrays of carbon nanotubes and their field emission properties.* Science, 1999. **283**(5401): p. 512-514.

51. Choi, W., et al., *Fully sealed, high-brightness carbon-nanotube field-emission display.* Applied physics letters, 1999. **75**(20): p. 3129-3131.

52. Peng, L.-M., Z. Zhang, and S. Wang, *Carbon nanotube electronics: recent advances.* Materials today, 2014. **17**(9): p. 433-442.

53. Qiu, C., et al., *Scaling carbon nanotube complementary transistors to 5-nm gate lengths.* Science, 2017. **355**(6322): p. 271-276.

54. Li, J., et al., *Carbon nanotube sensors for gas and organic vapor detection.* Nano letters, 2003. **3**(7): p. 929-933.

55. Yamada, T., et al., *A stretchable carbon nanotube strain sensor for human-motion*

detection. Nature nanotechnology, 2011. **6**(5): p. 296-301.

56. Wong, S.S., et al., *Single-walled carbon nanotube probes for high-resolution nanostructure imaging.* Applied Physics Letters, 1998. **73**(23): p. 3465-3467.

57. Akita, S., et al., *Carbon nanotube tips for a scanning probe microscope: their fabrication and properties.* Journal of Physics D: Applied Physics, 1999. **32**(9): p. 1044.

58. Cui, K., et al., *Self-assembled microhoneycomb network of single-walled carbon nanotubes for solar cells.* The Journal of Physical Chemistry Letters, 2013. **4**(15): p. 2571-2576.

59. Cui, K., et al., *Air-Stable High-Efficiency Solar Cells Using Improved Single-Walled Carbon Nanotube Films.*

60. Xu, J. and T.S. Fisher, *Enhancement of thermal interface materials with carbon nanotube arrays.* International Journal of Heat and Mass Transfer, 2006. **49**(9): p. 1658-1666.

61. Zhang, K., et al., *Carbon nanotube thermal interface material for high-brightness light-emitting-diode cooling.* Nanotechnology, 2008. **19**(21): p. 215706.

62. Tong, T., et al., *Dense vertically aligned multiwalled carbon nanotube arrays as thermal interface materials.* IEEE Transactions on Components and Packaging Technologies, 2007. **30**(1): p. 92-100.

63. Yang, F., et al., *Chirality-specific growth of single-walled carbon nanotubes on solid alloy catalysts.* Nature, 2014. **510**(7506): p. 522-524.

64. Yang, F., et al., *Growing zigzag (16, 0) carbon nanotubes with structure-defined catalysts.* Journal of the American Chemical Society, 2015. **137**(27): p. 8688-8691.

65. An, H., et al., *Chirality specific and spatially uniform synthesis of single-walled carbon nanotubes from a sputtered Co–W bimetallic catalyst.* Nanoscale, 2016. **8**(30): p. 14523-14529.

66. Si, J., et al., *Carbon Nanotube Self-Gating Diode and Application in Integrated Circuits.* ACS Nano, 2016. **10**(7): p. 6737-6743.

67. Nasibulin, A.G., et al., *Multifunctional free-standing single-walled carbon nanotube films.* ACS nano, 2011. **5**(4): p. 3214-3221.

68. Wu, Z., et al., *Transparent, conductive carbon nanotube films.* Science, 2004. **305**(5688): p. 1273-1276.

69. Feng, C., et al., *Flexible, stretchable, transparent conducting films made from superaligned carbon nanotubes.* Advanced Functional Materials, 2010. **20**(6): p. 885-891.

70. Behnam, A., et al., *High-field transport and thermal reliability of sorted carbon nanotube network devices.* ACS nano, 2012. **7**(1): p. 482-490.

71. Fukumaru, T., T. Fujigaya, and N. Nakashima, *Development of n-type cobaltocene-encapsulated carbon nanotubes with remarkable thermoelectric property.* Scientific reports, 2015. **5**.

72. Nakai, Y., et al., *Giant Seebeck coefficient in semiconducting single-wall carbon nanotube film.* Applied Physics Express, 2014. **7**(2): p. 025103.

73. Yanagi, K., et al., *Tuning of the thermoelectric properties of one-dimensional material networks by electric double layer techniques using ionic liquids.* Nano letters, 2014. **14**(11): p. 6437-6442.

74. Bell, L.E., *Cooling, heating, generating power, and recovering waste heat with thermoelectric systems.* Science, 2008. **321**(5895): p. 1457-1461.

75. Dresselhaus, M.S., et al., *New Directions for Low‐Dimensional Thermoelectric Materials.* Advanced Materials, 2007. **19**(8): p. 1043-1053.

76. Poehler, T.O. and H.E. Katz, *Prospects for polymer-based thermoelectrics: state of the art and theoretical analysis.* Energy & Environmental Science, 2012. **5**(8): p. 8110-8115.

77. Zhang, Q., et al., *Organic thermoelectric materials: Emerging green energy materials converting heat to electricity directly and efficiently.* Advanced Materials, 2014. **26**(40): p. 6829-6851.

78. Volkov, A.N. and L.V. Zhigilei, *Heat conduction in carbon nanotube materials: Strong effect of intrinsic thermal conductivity of carbon nanotubes.* Applied Physics Letters, 2012. **101**(4): p. 043113.

79. Qiu, L., et al., *Remarkably enhanced thermal transport based on a flexible horizontally-aligned carbon nanotube array film.* Scientific Reports, 2016. **6**: p. 21014.

80. Chen, S., et al., *Raman measurements of thermal transport in suspended monolayer graphene of variable sizes in vacuum and gaseous environments.* ACS nano, 2010. **5**(1): p. 321-328.

81. Balandin, A.A., et al., *Superior thermal conductivity of single-layer graphene.* Nano letters, 2008. **8**(3): p. 902-907.

82. Xu, X., et al., *Length-dependent thermal conductivity in suspended single-layer graphene.* Nature communications, 2014. **5**.

83. Wang, C., et al., *Superior thermal conductivity in suspended bilayer hexagonal boron nitride.* Scientific Reports, 2016. **6**: p. 25334.

84. Zhu, J., et al., *Ultrafast thermoreflectance techniques for measuring thermal conductivity and interface thermal conductance of thin films.* Journal of Applied Physics, 2010. **108**(9): p. 094315.

85. Greppmair, A., et al., *Measurement of the in-plane thermal conductivity by steady-state infrared thermography.* arXiv preprint arXiv:1608.00995, 2016.

86. Optris, I.T., *BASIC PRINCIPLES of non-contact temperature measurement*.

87. Rogalski, A., *HgCdTe infrared detector material: history, status and outlook.* Reports on Progress in Physics, 2005. **68**(10): p. 2267.

88. Shanks, H., et al., *Thermal conductivity of silicon from 300 to 1400 K.* Physical Review, 1963. **130**(5): p. 1743.

89. Yoshida, S., et al., *Morphology dependence of the thermal transport properties of single-walled carbon nanotube thin films.* Nanotechnology, 2017. **28**(18): p. 185701.

90. Vallabhaneni, A.K., et al., *Reliability of Raman measurements of thermal conductivity of single-layer graphene due to selective electron-phonon coupling: A first-principles study.* Physical Review B, 2016. **93**(12): p. 125432.

91. Seol, J.H., et al., *Two-dimensional phonon transport in supported graphene.* Science, 2010. **328**(5975): p. 213-216.

92. Mahan, G. and G.S. Jeon, *Flexure modes in carbon nanotubes.* Physical Review B, 2004. **70**(7): p. 075405.

93. Steiner, M., et al., *Phonon populations and electrical power dissipation in carbon nanotube transistors.* Nature Nanotechnology, 2009. **4**(5): p. 320-324.

94. Lian, F., *Thermal imaging and analysis of carbon nanotube composites.* Master Thesis, 2013: p. 1-37.

95. Maruyama, S., *A molecular dynamics simulation of heat conduction of a finite length single-walled carbon nanotube.* Microscale Thermophysical Engineering, 2003. **7**(1): p. 41-50.

96. Saito, R., et al., *Electronic structure of graphene tubules based on C 60.* Physical

Review B, 1992. **46**(3): p. 1804.

97. Thess, A., et al., *Crystalline ropes of metallic carbon nanotubes.* Science, 1996: p. 483-487.

98. Zhu, H.W., et al., *Direct Synthesis of Long Single-Walled Carbon Nanotube Strands.* Science, 2002. **296**(5569): p. 884-886.

99. Shi, Z., et al., *Mass-production of single-wall carbon nanotubes by arc discharge method.* Carbon, 1999. **37**(9): p. 1449-1453.

100. Journet, C., et al., *Large-scale production of single-walled carbon nanotubes by the electric-arc technique.* Nature, 1997. **388**(6644): p. 756-758.

101. Pettes, S.

102. Che, J., T. Cagin, and W.A. Goddard III, *Thermal conductivity of carbon nanotubes.* Nanotechnology, 2000. **11**(2): p. 65.

103. Padgett, C.W. and D.W. Brenner, *Influence of chemisorption on the thermal conductivity of single-wall carbon nanotubes.* Nano Letters, 2004. **4**(6): p. 1051-1054.

104. Grujicic, M., G. Cao, and B. Gersten, *Atomic-scale computations of the lattice contribution to thermal conductivity of single-walled carbon nanotubes.* Materials Science and Engineering: B, 2004. **107**(2): p. 204-216.

105. Zhang, G. and B. Li, *Thermal conductivity of nanotubes revisited: Effects of chirality, isotope impurity, tube length, and temperature.* The Journal of chemical physics, 2005. **123**: p. 114714.

106. Shiomi, J. and S. Maruyama, *Molecular dynamics of diffusive-ballistic heat conduction in single-walled carbon nanotubes.* Japanese Journal of Applied Physics-Part 1 Regular Papers and Short Notes, 2008. **47**(4): p. 2005-2009.

107. Feng, Y., J. Zhu, and D.-W. Tang, *Chirality and Diameter Influence on Thermal Conductivity of Single-Walled Carbon Nanotubes.* Journal of nanoscience and nanotechnology, 2015. **15**(4): p. 3092-3097.

108. Zhang, W., et al., *Chirality dependence of the thermal conductivity of carbon nanotubes.* Nanotechnology, 2004. **15**(8): p. 936-939.

109. Wingert, M.C., et al., *Thermal conductivity of Ge and Ge–Si core–shell nanowires in the phonon confinement regime.* Nano letters, 2011. **11**(12): p. 5507-5513.

110. Hippalgaonkar, K., et al., *Fabrication of microdevices with integrated nanowires*

for investigating low-dimensional phonon transport. Nano letters, 2010. **10**(11): p. 4341-4348.

111. Wingert, M.C., et al., *Sub-Amorphous Thermal Conductivity in Ultra-Thin Crystalline Silicon Nanotubes.* Nano Letters, 2015.

112. Inoue, T., et al., *Effect of gas pressure on the density of horizontally aligned single-walled carbon nanotubes grown on quartz substrates.* The Journal of Physical Chemistry C, 2013. **117**(22): p. 11804-11810.

113. Murakami, Y., et al., *Growth of vertically aligned single-walled carbon nanotube films on quartz substrates and their optical anisotropy.* Chemical Physics Letters, 2004. **385**(3): p. 298-303.

114. Yu, C., et al., *Thermal contact resistance and thermal conductivity of a carbon nanofiber.* Journal of heat transfer, 2006. **128**(3): p. 234-239.

115. Moore, A.L. and L. Shi, *On errors in thermal conductivity measurements of suspended and supported nanowires using micro-thermometer devices from low to high temperatures.* Measurement Science and Technology, 2010. **22**(1): p. 015103.

116. Yang, J., et al., *Measurement of the intrinsic thermal conductivity of a multiwalled carbon nanotube and its contact thermal resistance with the substrate.* Small, 2011. **7**(16): p. 2334-2340.

117. Prasher, R., *Predicting the thermal resistance of nanosized constrictions.* Nano letters, 2005. **5**(11): p. 2155-2159.

118. Libbrecht, K., E. Black, and C. Hirata, *A basic lock-in amplifier experiment for the undergraduate laboratory.* American Journal of Physics, 2003. **71**(11): p. 1208-1213.

119. Pettes, M.T., *Experimental Investigations of Thermal Transport in Carbon Nanotubes, Graphene, and Nanoscale Point Contacts.* PHD dissertation.

120. Shih, L., *Mesoscopic thermophysical measurements of microstructures and carbon nanotubes*. 2001: University of California, Berkeley.

121. Osman, M.A. and D. Srivastava, *Temperature dependence of the thermal conductivity of single-wall carbon nanotubes.* Nanotechnology, 2001. **12**(1): p. 21.

122. Inoue, T., et al., *Chirality analysis of horizontally aligned single-walled carbon nanotubes: decoupling populations and lengths.* Journal of Materials Chemistry A, 2015. **3**(29): p. 15119-15123.

123. Ong, Z.-Y. and E. Pop, *Molecular dynamics simulation of thermal boundary*

conductance between carbon nanotubes and SiO2. Physical Review B, 2010. **81**(15): p. 155408.

124. Prasher, R., *Thermal boundary resistance and thermal conductivity of multiwalled carbon nanotubes.* Physical Review B, 2008. **77**(7): p. 075424.

125. Shi, L., et al., *Thermal probing of energy dissipation in current-carrying carbon nanotubes.* Journal of Applied Physics, 2009. **105**(10): p. 104306.

126. Chang, C.-W., et al., *Breakdown of Fourier's law in nanotube thermal conductors.* Physical review letters, 2008. **101**(7): p. 075903.

127. Hsu, I.-K., et al., *Optical absorption and thermal transport of individual suspended carbon nanotube bundles.* Nano letters, 2009. **9**(2): p. 590-594.

128. Lindsay, L., D. Broido, and N. Mingo, *Lattice thermal conductivity of single-walled carbon nanotubes: Beyond the relaxation time approximation and phonon-phonon scattering selection rules.* Physical Review B, 2009. **80**(12): p. 125407.

129. Cao, J., et al., *Thermal conductivity of zigzag single-walled carbon nanotubes: Role of the umklapp process.* Physical Review B, 2004. **69**(7): p. 073407.

130. Hsu, I.-K., et al., *Optical measurement of thermal transport in suspended carbon nanotubes.* Applied Physics Letters, 2008. **92**(6): p. 63119-63119.

131. Kodama, T., et al., *Modulation of thermal and thermoelectric transport in individual carbon nanotubes by fullerene encapsulation.* Nature materials, 2017.

132. Zhang, Z.M.Z.M., *Nano/microscale heat transfer*. 2007.

LIST OF FIGURES

LIST OF TABLES

NOMENCLATURE

CNT	carbon nanotube
SWNT	single walled carbon nanotube
TCR	temperature coefficient of resistance
RIE	reactive ion etching
DRIE	deep reactive ion etching
EBL	electron beam lithography
PL	photolithography
DOS	density of states
IR	infrared
ACCVD	alcohol catalyst chemical vapor deposition
NEG	noise equivalent thermal conductance
HASWNT	horizontally aligned single walled carbon nanotube
TEM	tansmission electron microscope
TBR	thermal boundary resistance
SEM	scanning electron microscope
RT	room temperature

ACKNOWLEGEMENTS

I can hardly step forward without help from many people during this doctorate journey. Firstly, I would like to express my sincere gratitude to my supervisor, Maruyama-Sensei, who encourages me all the way to finally fulfill the doctorate degree.

I am very fortunate to meet and discuss with all the previous and current members in Maruyama-Chiashi Lab. Chiashi-Sensei is humorous and provides useful advices for presentation; Xiang Rong-San is the master of TEM and also gives me good suggestions; Inoue-San helps me everything possible about experiments. I also appreciate the support from Technician Watanabe-San, Secretaries Terao-San and Shimada-San. Moreover, all the other members that we share laughter and bitterness in research or life are so precious to me.

I would like to thank our collaborators, Prof. Esko Kauppinen from Aalto University for providing SWNT thin film samples; Prof. Shi Li from The University of Texas at Austin for examining the micro-thermometer measurement setup; Takeda Technical Assistant Eric Lebrasseur, who taught me everything about MEMS fabrication, and also Takeda Technical Assistants Fujiwara-San and Okamoto-San to solve my puzzles in Takeda Clean Room.

Last but not the least, I would like to show my thankful heart to my loving parents, supporting sisters and friends, lovely and joyful nephew and niece

CURRICULUM VITAE

Education Background

October 2014-present

Ph. D. candidate, Department of Mechanical Engineering, The University of Tokyo, Japan

Advisor: Prof. Shigeo Maruyama

September 2011 – July 2014

Master of Engineering, Institute of Engineering Thermophysics, Chinese Academy of Sciences, China

Advisor: Prof. Dawei Tang

September 2007 – July 20011

Bachelor of Engineering, School of Energy and Power Engineering, Huazhong University of Science and Technology, China

Personal Information

E-mails : fengya@photon.t.u-tokyo.ac.jp; ethelfeng@gmail.com

Current Address: Department of Mechanical Engineering, School of Engineering, The University of Tokyo Room 63C2, Engineering Bldg. 2, 7-3-1 Hongo, Bunkyo-ku, Tokyo 113-8656, Japan